Ligand Exchange and Spin State Equilibria of Fe-II(N4Py) and Related Complexes in Aqueous Media

Draksharapu, Apparao; Li, Qian; Logtenberg, Hella; van den Berg, Tieme A.; Meetsma, Auke; Killeen, J. Scott; Feringa, Ben L.; Hage, Ronald; Roelfes, Gerard; Browne, Wesley R.

Published in:
Inorganic Chemistry

DOI:
10.1021/ic201879b

Supporting online information

Ligand exchange and spin state equilibria of Fe^{II}(N4Py) and related complexes in aqueous media

Apparao Draksharapu, Qian Li, Hella Logtenberg, Tieme A. van den Berg, Auke Meetsma, J. Scott Killeen, Ben L. Feringa, Ronald Hage, Gerard Roelfes, Wesley R. Browne*

Table of Contents

1. Synthesis and characterization of ligands and complexes

Caution! *Perchlorate salts of metal complexes incorporating organic ligands are potentially explosive. These compounds should be prepared in small quantities and handled with suitable protective safe guards.*

d_5-1,1-di(pyridin-2-yl)-*N*,*N*-bis(pyridin-2-ylmethyl)methanamine d_5-N4Py. N4Py (100 mg, 0.27 mmol) was dissolved in 3 ml of CH_3COOD. The solution was heated under reflux. After 3 h the solvent was evaporated *in vacuo* and CH_2Cl_2 was added to the residue. The CH_2Cl_2 solution was washed with sat. $NaHCO_3$. The aqueous layer was washed with CH_2Cl_2. The combined CH_2Cl_2 layers were washed with brine and dried (over anhydrous Na_2SO_4). Evaporation of the solvent afforded d_5-N4Py (85 mg, 0.23 mmol, 84 %) as a yellow oil. Extent of deuteration was 95% as determined by ^{1}H NMR spectroscopy.

$[Fe^{II}(d_5\text{-N4Py})(CH_3CN)](ClO_4)_2.2H_2O$ (d_5-1). A solution of $Fe(ClO_4)_2{\cdot}6H_2O$ (92 mg, 0.25 mmol) in CH_3CN (3 ml) was added to a solution of d_5-N4Py (85 mg, 0.23 mmol) in methanol (3 ml). The solution was placed in an ethyl acetate bath and after two days **d_5-1** (119 mg, 0.17 mmol, 74.5 %) was obtained as dark red crystals. ^{1}H NMR (CD_3CN) δ 7.09 (d, 2H), 7.39 (m, 4H), 7.70 (m, 2H), 7.94 (m, 4H), 8.92 (d, 2H), 9.06 (d, 2H). (see Figure S 6)

1,1-di(pyridin-2-yl)-*N*,*N*-bis(pyridin-2-ylmethyl)ethanamine (MeN4Py). N4Py (181 mg, 0.49 mmol) was dissolved in ether/THF (20 ml, 3:1) under an argon atmosphere. The solution was cooled to -80 °C and *t*-butyl lithium (0.36 ml of a 1.5 M solution in pentane, 1.1 equiv) was added. After stirring for 15 min at -80 °C, iodomethane (45 µl, 1.5 mmol) was added. The mixture was allowed to warm to room temperature overnight. The solvent was removed *in vacuo* and water was added (5 ml). The aqueous mixture was extracted with dichloromethane (3 x 15 ml) and the combined organic layers were washed with brine, dried (Na_2SO_4) and the solvent removed *in vacuo* to yield MeN4Py (158 mg, 0.42 mmol, 84 %) as a white solid. An analytically pure sample was obtained by recrystallization from hexane/ethyl acetate, m.p. 152.7-152.9 °C. ^{1}H NMR ($CDCl_3$) δ 2.05 (s, 3H), 3.96 (s, 4H), 6.89 (m, 2H),

7.07 (m, 2H), 7.39 (m, 4H), 7.62 (m, 2H), 8.02 (m, 2H), 8.31 (m, 2H), 8.53 (m, 2H); ^{13}C NMR ($CDCl_3$) δ 21.20 (q), 58.40 (t), 73.10 (s), 121.19 (d), 121.58 (d), 123.31 (d), 123.47 (d), 135.54 (d), 135.91 (d), 148.49 (d), 148.59 (d), 160.87 (s), 163.99 (s); Anal. calcd for $C_{24}H_{23}N_5$: C 75.56, H 6.08, N 18.36; Found: C 75.34, H 6.12, N 18.30. ESI-MS; 382.02 (calc. MH+ 382.026)

[Fe^{II}(MeN4Py)(CH_3CN)](ClO_4)$_2$ (2). A solution of $Fe(ClO_4)_2 \cdot 6H_2O$ (112 mg, 0.31 mmol) in CH_3CN (3 ml) was added to a solution of MeN4Py (90 mg, 0.24 mmol) in methanol (3 ml). The solution was placed in an ethyl acetate bath and after 2 days **2** (111 mg, 0.16 mmol, 69 %) was obtained as dark red crystals. Crystals suitable for X-ray analysis were obtained by slow vapor diffusion of ethyl acetate into an acetonitrile solution of **2**. ^{1}H NMR (CD_3CN) δ 2.27 (s, 2H), 4.17 ($q_{(AB)}$, 4H, J = 17.9 Hz), 7.02 (m, 2H), 7.34 (m, 4H), 7.67 (m, 4H), 7.94 (m, 2H), 8.91 (d, 2H, J = 5.5 Hz), 9.0 (d, 2H, J = 5.5 Hz); Anal. calcd for $C_{26}H_{26}Cl_2FeN_6O_8$: C 46.11, H 3.87, N 12.41; Found: C 46.11, H 3.54, N 12.41.

2. X- Ray Crystallography

A red, needle-shaped crystal (0.1 × 0.1 × 0.6 mm) of **2**, was cut from a larger aggregate. Data were collected on an Enraf-Nonius CAD4 Turbo diffractometer on a rotating anode (13033 Reflections measured, 3335 independent reflections). An empirical extinction correction, based on measured ψ-scan data, was applied. The structure was solved by Patterson methods (SHELXS 86) and refined on F^2 using SHELXL-97. One of the ClO_4^- ions is located on a mirror plane and is ordered; the other one is located on a twofold rotation axis and is disordered over two positions. Mild bond length restraints were applied to the disordered bonds. All non-hydrogen atoms were refined with anisotropic thermal parameters; hydrogen atoms were included in the refinement on calculated positions riding on their carrier atoms. Hydrogen atoms were refined with a fixed isotropic thermal parameter related to the value of the equivalent isotropic displacement parameter of their carrier atoms.

The crystal of **3** used, with an irregular fragment shape with the dimensions of 0.39 x 0.23 x 0.21 mm was picked from the mother liquor, to avoid a deterioration and glued directly on a glass fiber and transferred into the cold nitrogen stream of the low temperature unit mounted on the diffractometer and aligned on a *Bruker APEX-II CCD* area-detector diffractometer (Platform with full three-circle goniometer). The diffractometer was equipped with a 4K *CCD* detector set 60.0 mm from the crystal. The crystal was cooled to 100(1) K using the *Bruker KRYOFLEX* low-temperature device. Intensity measurements were performed using graphite monochromated Mo-K$\overline{\alpha}$ radiation from a sealed ceramic diffraction tube (*SIEMENS*). Generator settings were 50 KV/ 40 mA. *APEX-II* was used for preliminary determination of the unit cell constants and data collection control. The intensities of reflections of a hemisphere were collected by a combination of 3 sets of exposures (frames). Each set had a different ϕ angle for the crystal and each exposure covered a range of 0.3° in ω. A total of 1800 frames were collected with an exposure time of 20.0 seconds per frame. The overall data collection time was 16.0 h. Data integration and global cell refinement was performed with the program *SAINT*. The final unit cell was obtained from the *xyz* centroids of 8352 reflections after integration. Intensity data were corrected

for Lorentz and polarization effects, scale variation, for decay and absorption: a multi-scan absorption correction was applied, based on the intensities of symmetry-related reflections measured at different angular settings (*SADABS*), and reduced to F_o^2. The program suite *SAINT* was used for space group determination (*XPREP*). CCDC no. for **3**: 842062

Table S1. Crystallographic data for complexes **1-3**

	1[1]	**2**	**3**
Empirical formula	$C_{26}H_{28}Cl_2FeN_6O_9$	$C_{26}H_{26}Cl_2FeN_6O_8$	$C_{28}H_{28}Cl_2FeN_6O_8$
fw (g mol^{-1})	695.30	677.28	703.32
cryst syst	monoclinic	orthorhombic	triclinic
space group	$P2_1/n$	Ima2	*P*-1
a (Å)	12.191(1)	15.626(3)	10.7655(4)
b (Å)	18.500(1)	12.0088(13)	12.2949(4)
c (Å)	13.015(1)	14.9414(19)	13.1002(5)
α (deg)	90	90	83.632(2)
β (deg)	95.928(8)	90	73.912(2)
γ (deg)	90	90	65.569(2)
V ($Å^3$)	2919.6(4)	2803.7(7)	1516.86(10)
Z	4	8	2
D_{calc} (g cm^{-3})	1.582	1.6045(4)	1.408
T (K)	130	150	100(1)
λ (Å)	0.71073	0.71073	0.71073
μ (cm^{-1})	7.6	7.9	7.23
R_F[a]	0.046	0.035	0.0333
R_w[b]	0.049	-	-
wR2[c]	-	0.086	0.0873

[a] $R_F = \sum(||F_o| - |F_c||)/\sum|F_o|$. [b] $R_w = [\sum(w(|F_o| - |F_c|)^2)/\sum w|F_o|^2]^{1/2}$. [c] $wR2 = [\sum[w(F_o^2 - F_c^2)^2]/\sum[w(F_o^2)^2]]^{1/2}$.

3. FTIR and non-resonant Raman Spectroscopy

FTIR spectra were recorded using a UATR (ZnSe) with a Perkin Elmer Spectrum400, equipped with a liquid nitrogen cooled MCT detector. Raman spectra were recorded at λ_{exc} 785 nm using a Perkin Elmer Raman Station at room temperature. Raman spectra were obtained with excitation at 400.8 (50 mW at source, PowerTechnology), 449 nm (35 mW at source, PowerTechnology), 473 (100 mW at source, Cobolt Lasers), and 355 nm (10 mW, Cobolt Lasers) to the sample through a 5 cm diameter plano-convex lens (f = 6 cm) and Raman scattering collected in a 180^o backscattering arrangement. The collimated Raman scattering was focused by a second 5 cm diameter plano convex lens (f = 6 cm) through an appropriate long pass edge filter (Semrock) into a Shamrock300i spectrograph (Andor Technology) with a 1200 L/mm grating blazed at 500 nm, or 2400 L/mm blazed at 400 nm and acquired with an DV420A-BU2 CCD camera (Andor Technology). The spectral slit width was set to 10 or 20 μm. Each spectrum was accumulated, typically 60 or 120 times with 5 s acquisition time, resulting in a total acquisition time of between 5 to 10 min per spectrum. Data were recorded and processed using Solis (Andor Technology) with spectral calibration performed using the Raman spectrum of acetonitrile/toluene 50:50 (v:v). Samples were held in quartz 10 mm path length cuvettes. For pH dependent resonance Raman studies Na_2SO_4 was added as internal standard in water and aqueous $HClO_4$ or NaOH solutions were employed to adjust the pH. The UV/Vis absorption spectra were recorded before and after each Raman measurement to verify that no change had taken place during the measurement. Baseline correction was performed for all spectra. The concentrations used for resonance Raman studies were 0.05-0.5 mM for all samples in acetonitrile and water. At 785 nm (non-resonant) Raman spectra were recorded using 1 M solutions.The solid state Raman spectra of complex **1**, **2**, **3** and d_5-**1** are shown in Figure S1. The solid state Raman spectrum of **1**, shows the expected mode of the CH_3CN ligand at 2273 cm^{-1} in addition to the modes of the N4Py ligand. Overall the spectrum is consistent with polypyridyl complexes such as $[Fe(bpy)_3]^{2+}$.[2] The most notable differences are observed in the region 600-1300 cm^{-1} and are assigned to the alkyl amine backbone on the basis of comparison with d_5-**1** (Figure S1).[3]

The Raman spectra (recorded under non-resonant conditions at λ_{exc} 785 nm) of both crystalline material and a 1 M solution in acetonitrile of **1** (Figure S4) and of **2** (Figure S5) are (with the exception of solvent bands) identical both in terms of wavenumber and relative intensity of the modes. The nitrile stretch of the CH_3CN ligand of **1** and **2** in the solid state at 2273 cm^{-1} and 2269 cm^{-1}, respectively, are observed at the same wavenumber in solution also. This data confirm that the structure of complexes **1** and **2**, *i.e.* the pentadentate coordination of the N4Py ligand to the Fe^{II} center, is retained in acetonitrile solution.

In the case of **3** in the solid state the symmetric nitrile stretch of the coordinated CH_3CN ligand is observed at 2285 cm^{-1}, and the asymmetric stretch at 2320 cm^{-1} (Figure S 1). The symmetric stretch of **3** is 12 cm^{-1} higher and relatively more intense than for **1**. The blue-shift, of the bound CH_3CN nitrile mode on going from **1** to **3** indicates a decrease in backbonding to the acetonitrile ligand and hence a change in electron density on the Fe^{II} centers (*i.e.* increase in $E_{½}$, *vide infra*). The differences between the vibrational spectra of **1-3** reflect the differences in the positioning of the ligand around the metal center in both complexes.

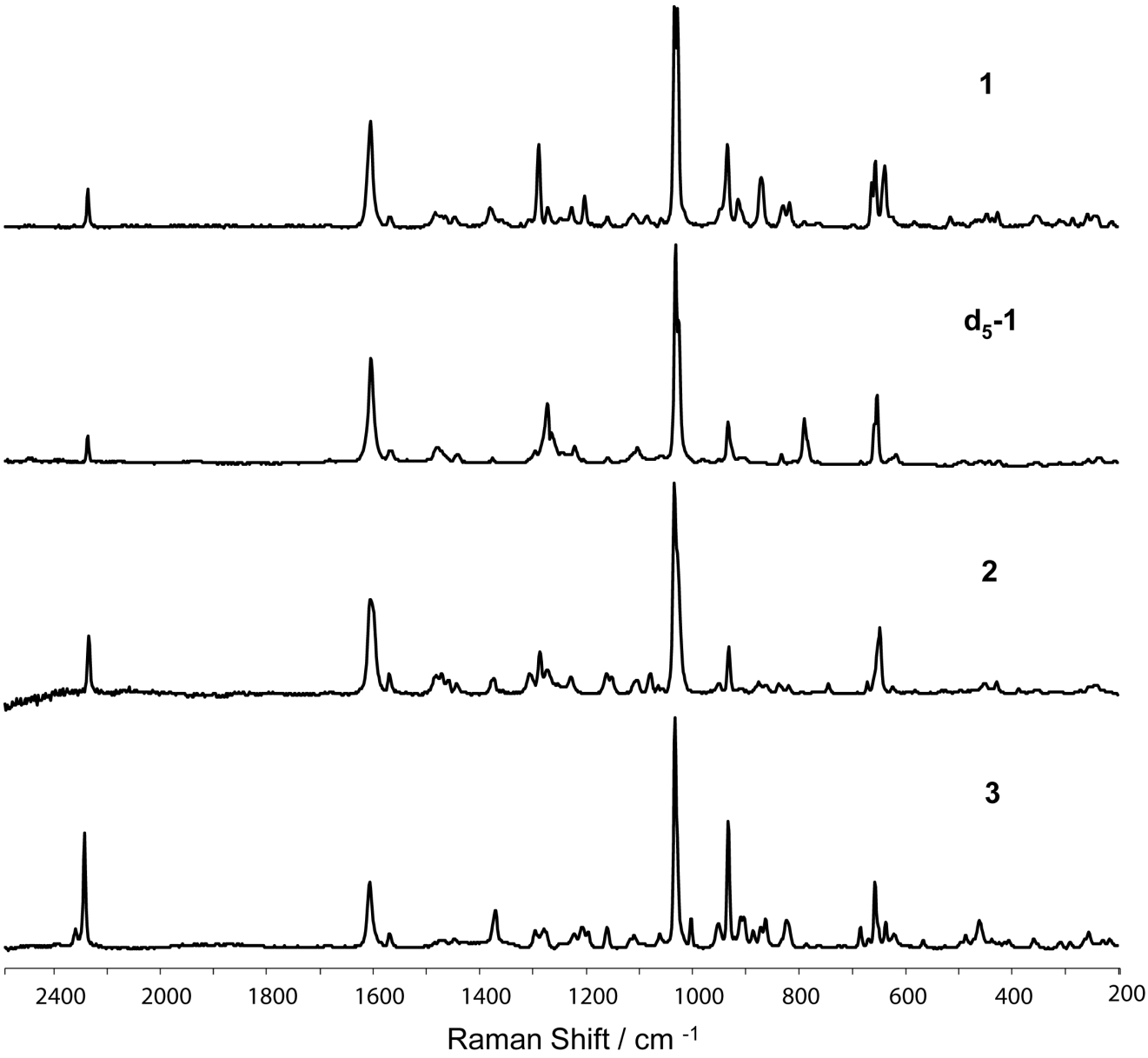

Figure S 1 Solid state Raman spectra of **1**, **d_5-1**, **2** and **3** at λ_{exc} 785 nm.

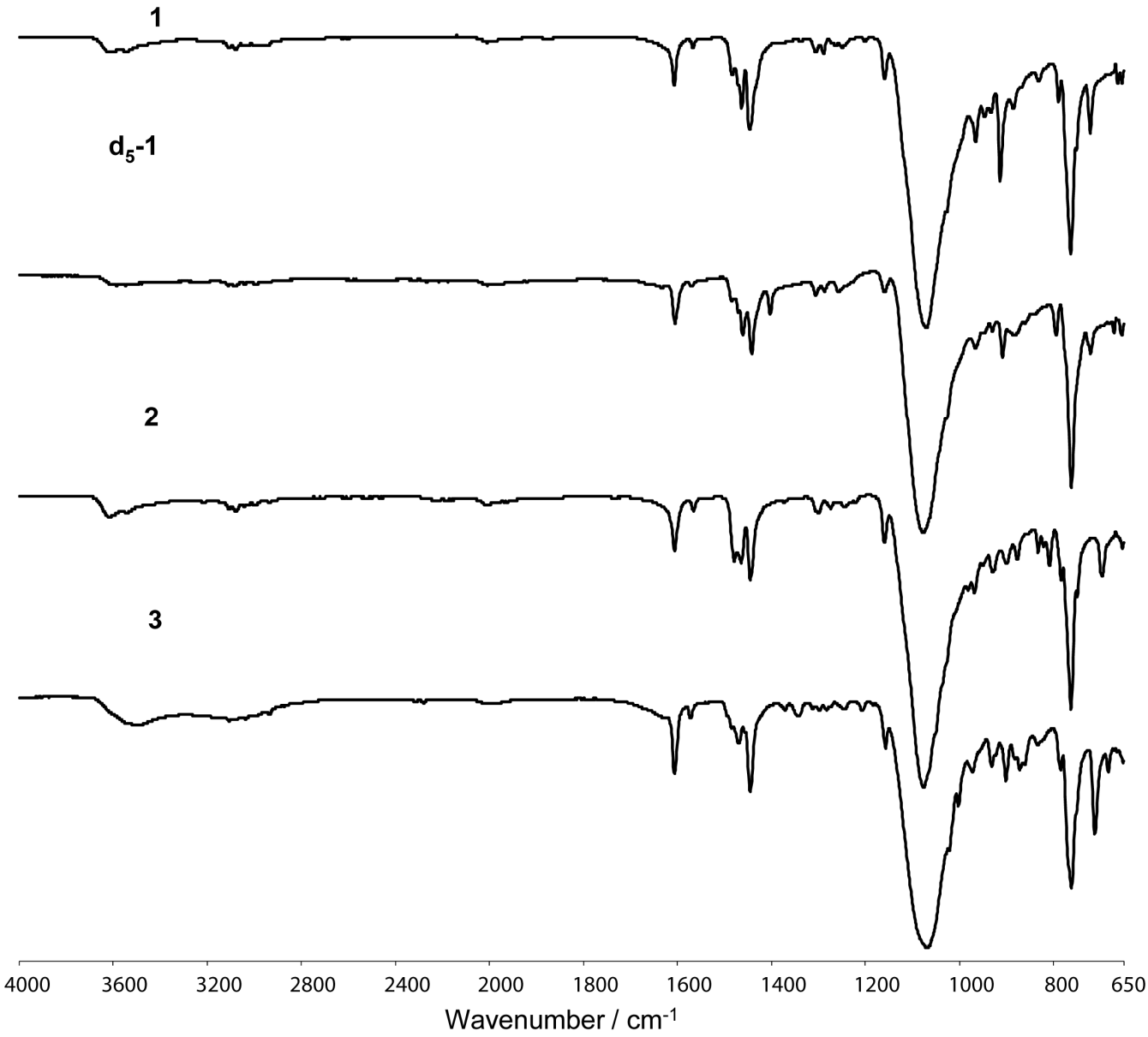

Figure S 2 FTIR spectra of complexes **1, d$_5$-1**, **2** and **3**.

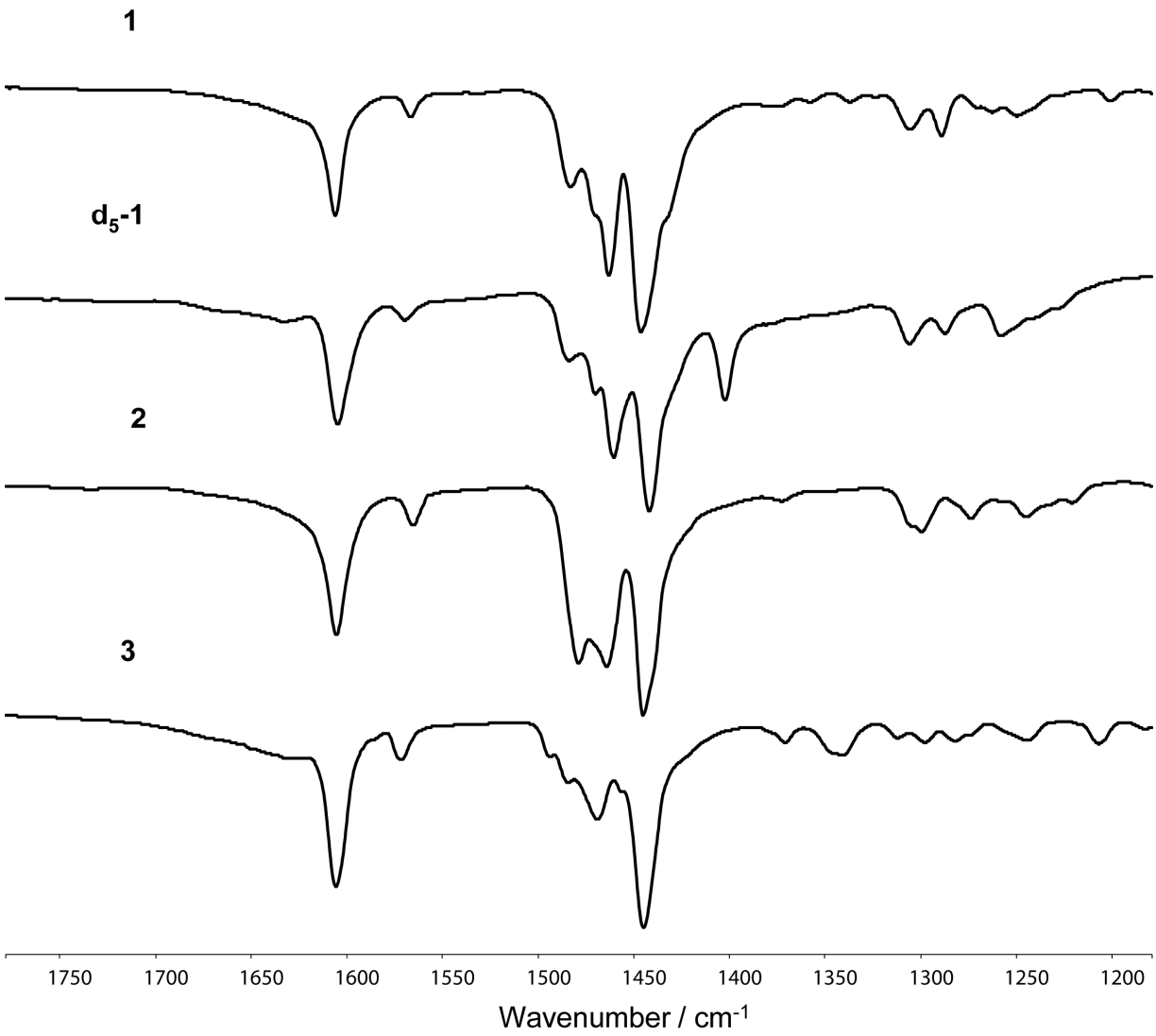

Figure S 3 FTIR spectra (fingerprint region) of complexes **1, d_5-1**, **2** and **3**.

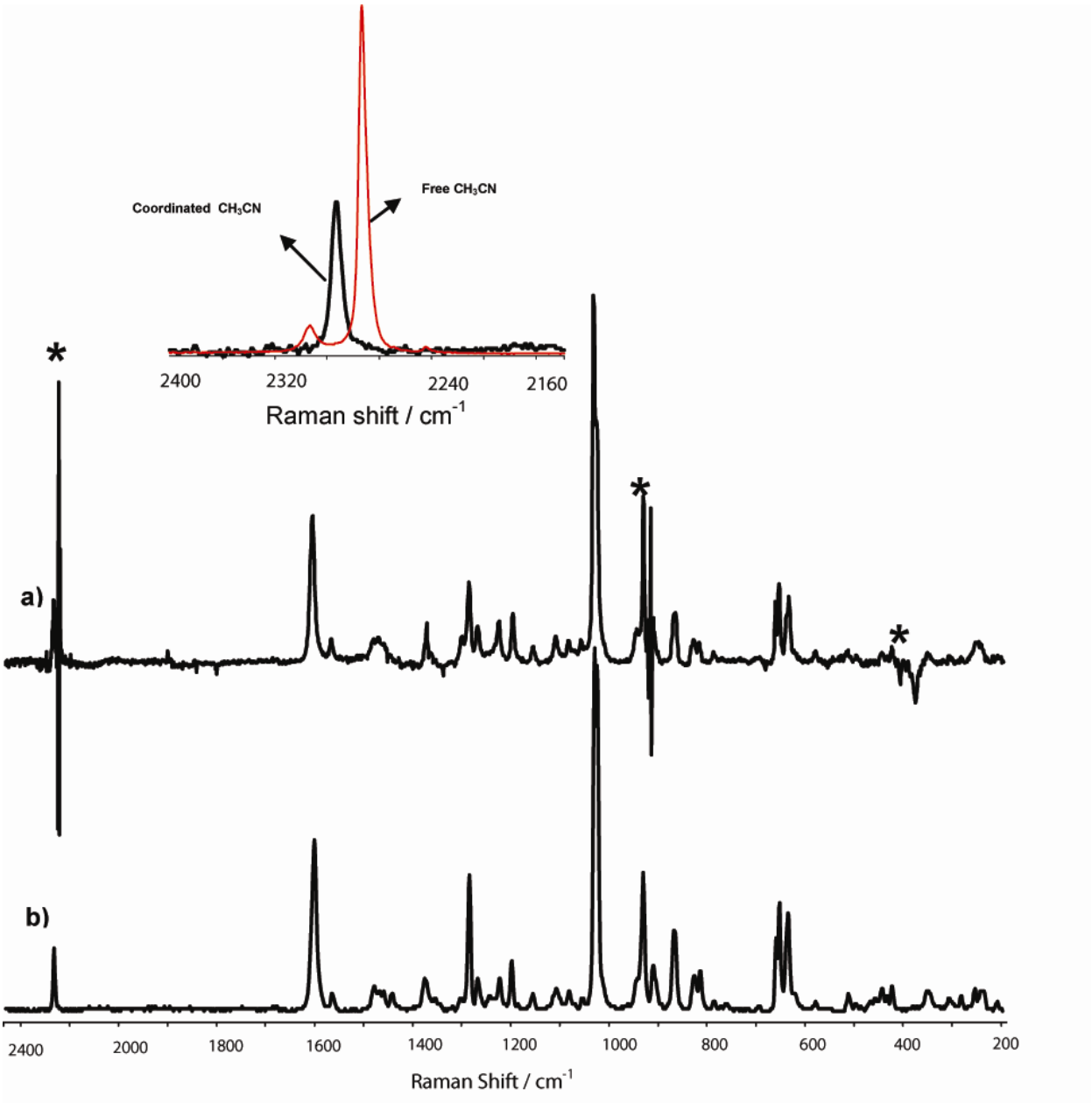

Figure S 4 Raman spectra of **1** a) 1 M in acetonitrile (solvent subtracted) b) as a solid powder. λ_{exc} 785 nm. Insert. C≡N vibrational bands of the CH_3CN ligand coordinated to the Fe^{II} center in complex **1** (black), and of acetonitrile solvent (red). * artifact from solvent subtraction.

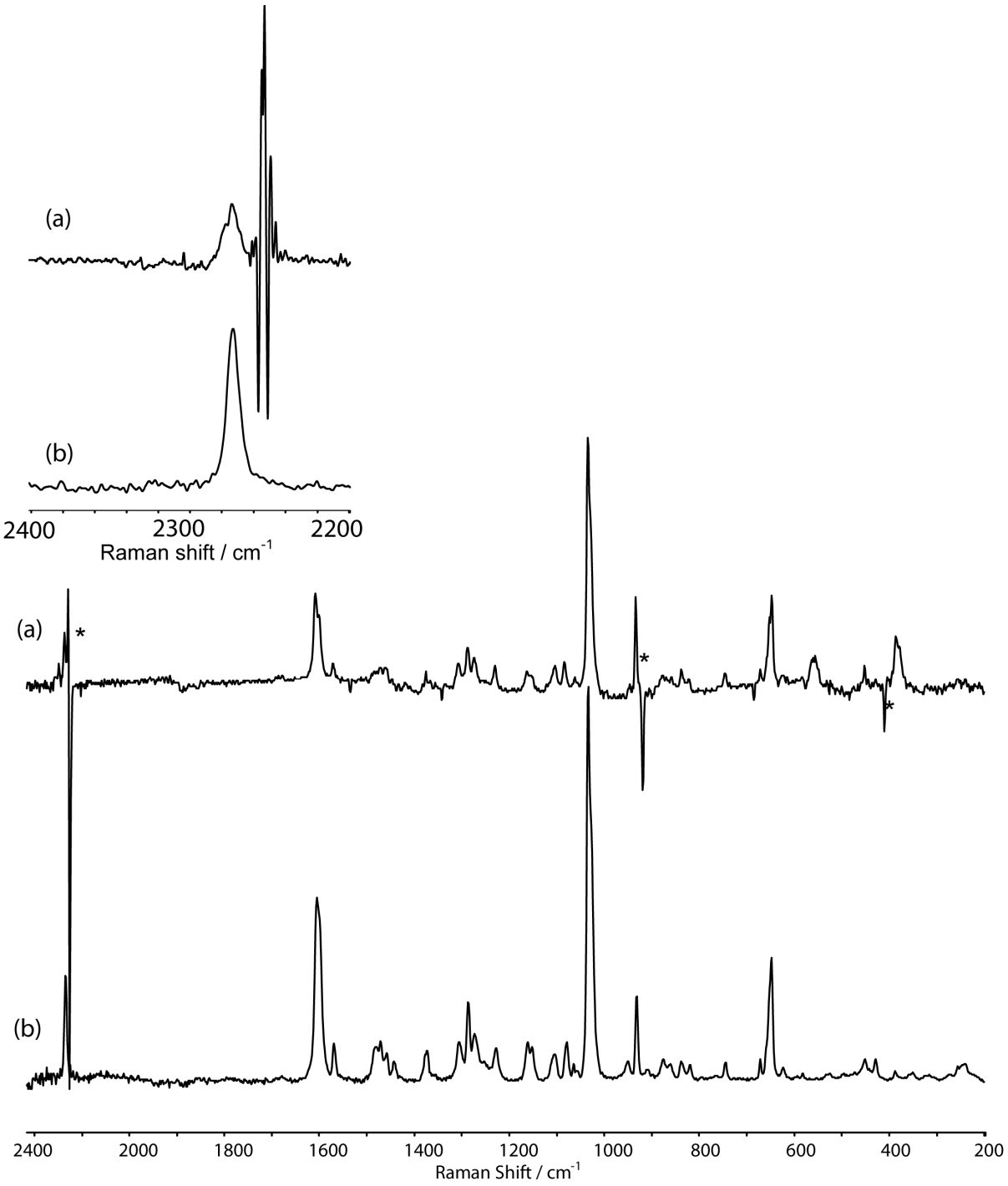

Figure S 5 Raman spectra of **2** a) 1 M in acetonitrile (solvent subtracted) and b) as a solid powder. λ_{exc} 785 nm. * artifact from solvent subtraction. Insert: expansion of the region from 2200 to 2400 cm^{-1}.

4. ^{1}H NMR spectroscopy

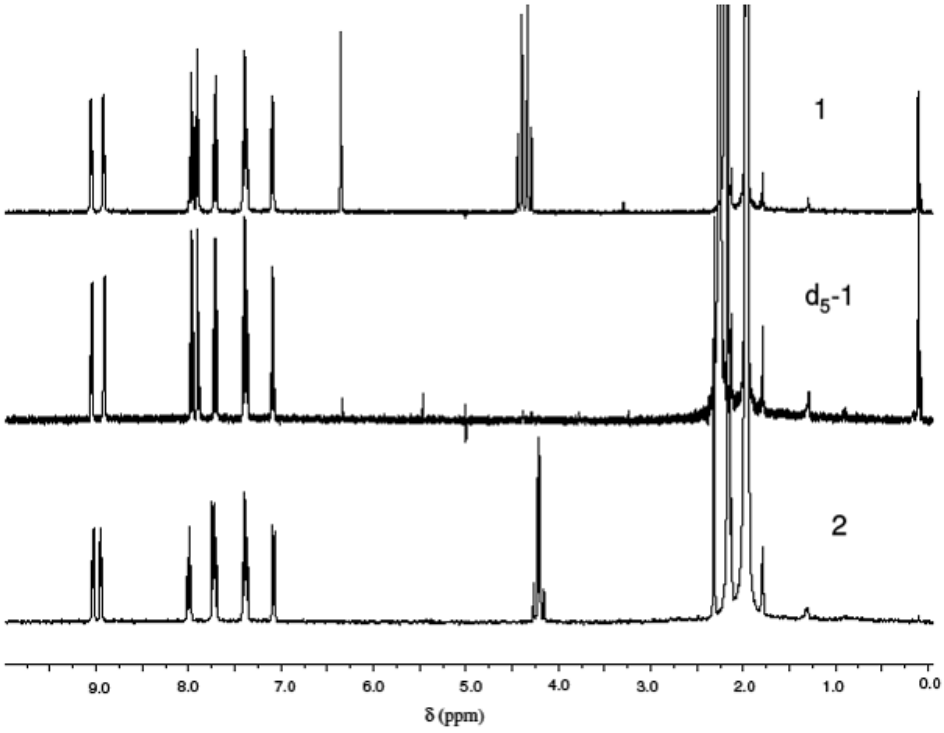

Figure S 6 ^{1}H NMR spectra of **1**, d_5-**1** and **2** in CD_3CN.

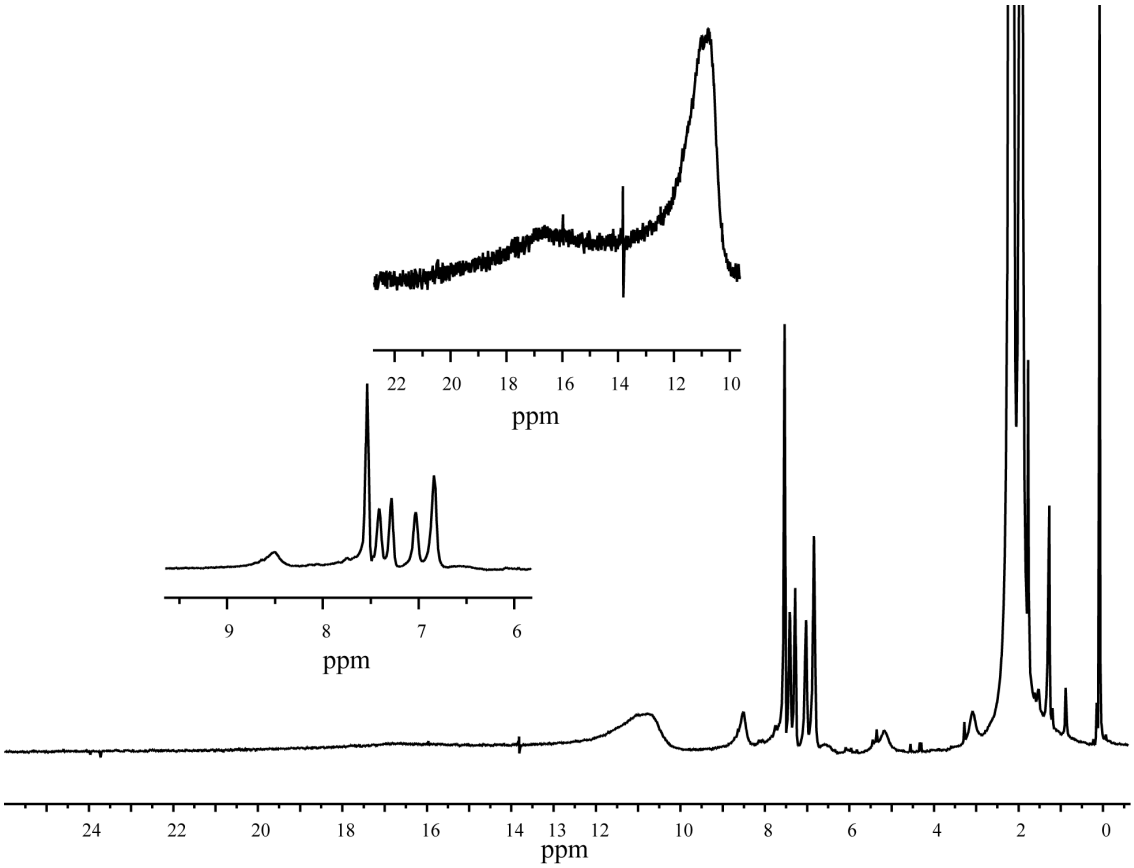

Figure S 7 ^{1}H NMR spectra of **3** in CD_3CN expansions shown as insets for clarity. Note that the spectrum is highly sensitive to traces of water with increasing paramagnetic character as the water content increases.

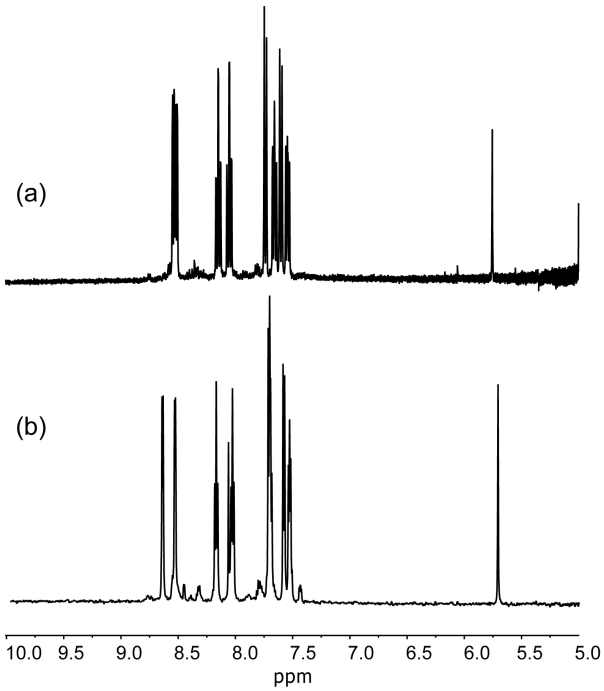

Figure S 8 ^{1}H NMR spectra of (a) N4Py at pD 1.86 and (b) **1** at pD 1.94 in D_2O.

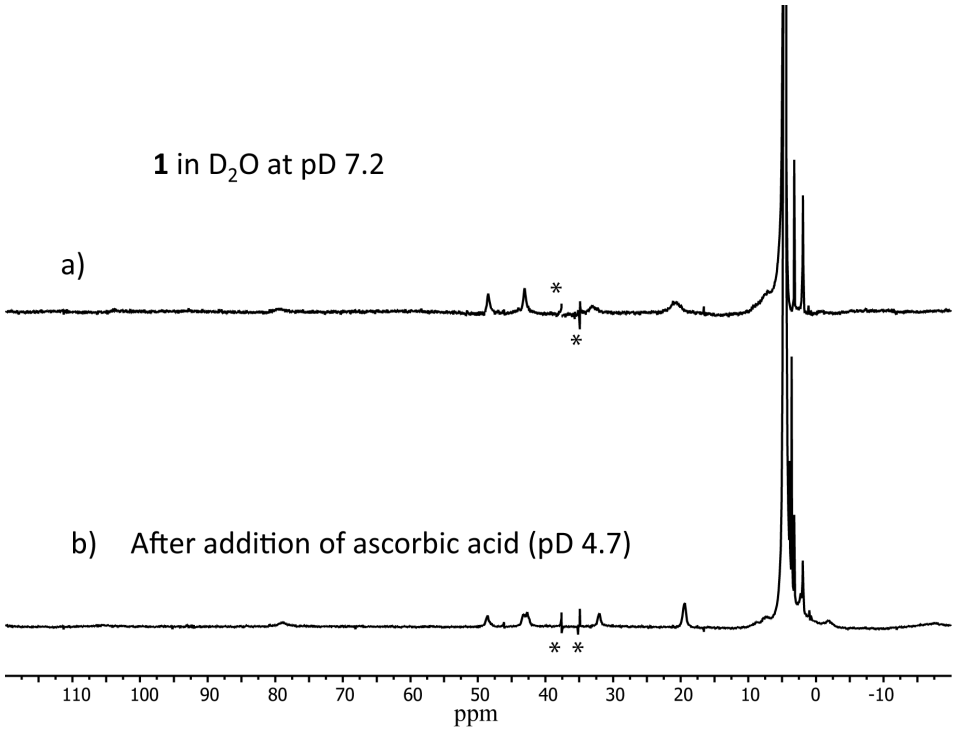

Figure S 9 ^{1}H NMR spectra of **1** in D_2O (a) pD 7.2 without ascorbic acid and (b) at pD 4.7 with excess ascorbic acid. (note that the sharp signals indicated by * are spectral artifacts). Fe^{II}/Fe^{III} self-exchange reactions can be excluded as the source of line broadening based on the absence of an effect of addition of the reduction ascorbic acid to a solution of **1** in D_2O.

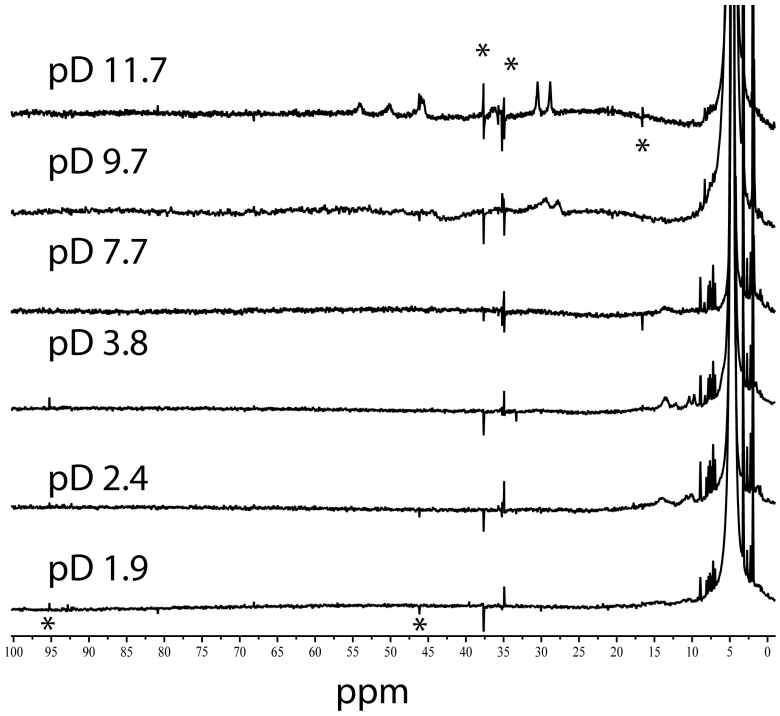

Figure S 10 pD dependence of the ^{1}H NMR spectrum of **2** in D_2O (note that the sharp signals indicated by * are spectral artifacts).

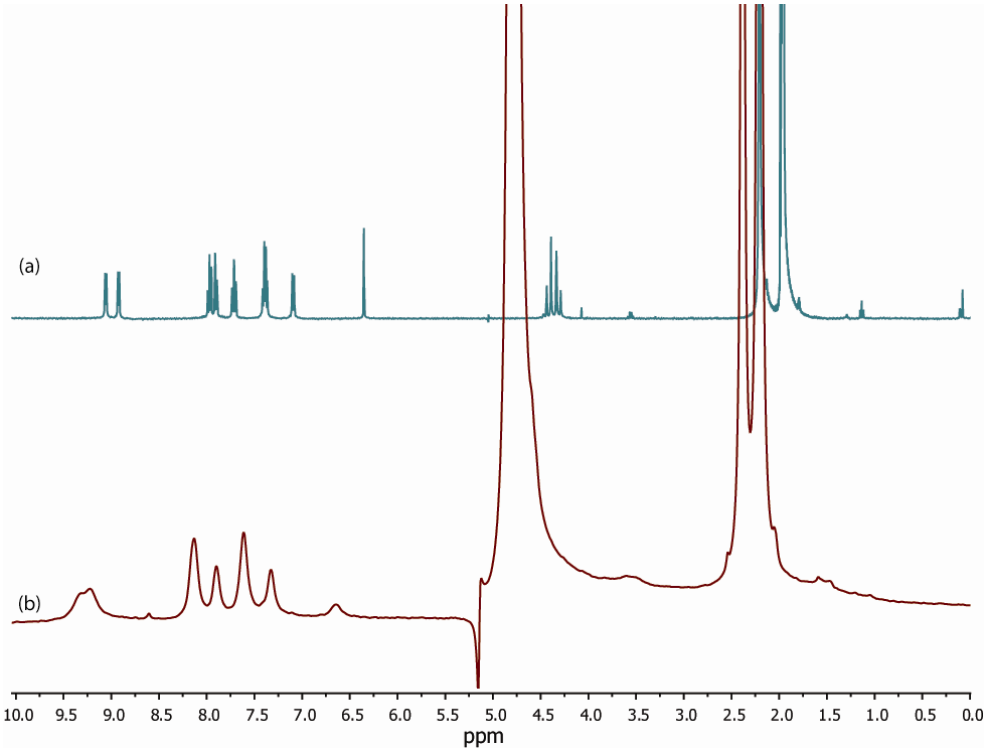

Figure S 11 ^{1}H NMR spectra of **1** (a) in CD_3CN and (b) in D_2O at pD 6.5 with 1 vol% acetonitrile added.

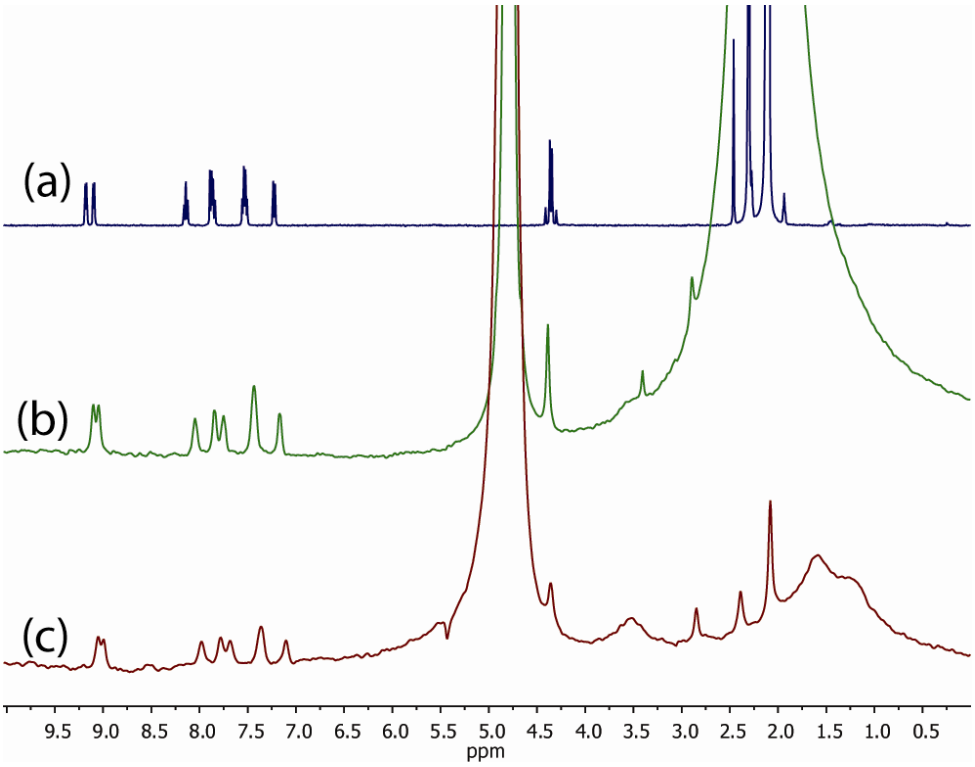

Figure S 12 ^{1}H NMR spectra of **2** (a) in CD_3CN, (b) in D_2O at pD 6.5 with CH_3CN 1 vol% and (c) in D_2O at pD 6.5.

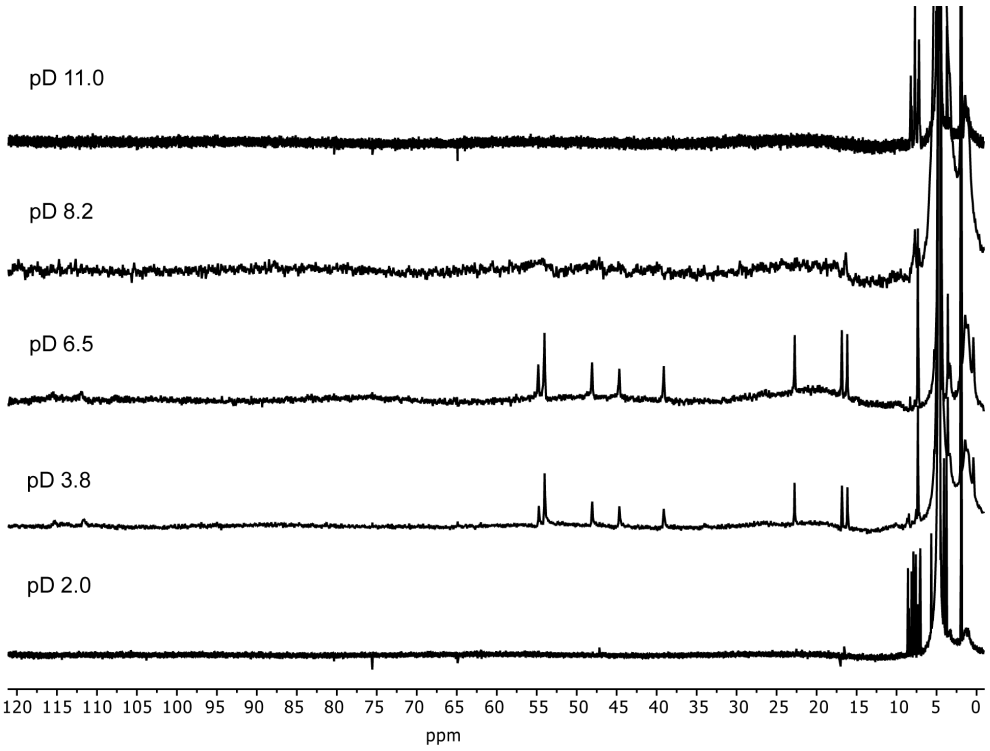

Figure S 13 ^{1}H NMR (400 MHz) spectra of **3** in D_2O at various pD values.

5. UV/Vis absorption spectroscopy

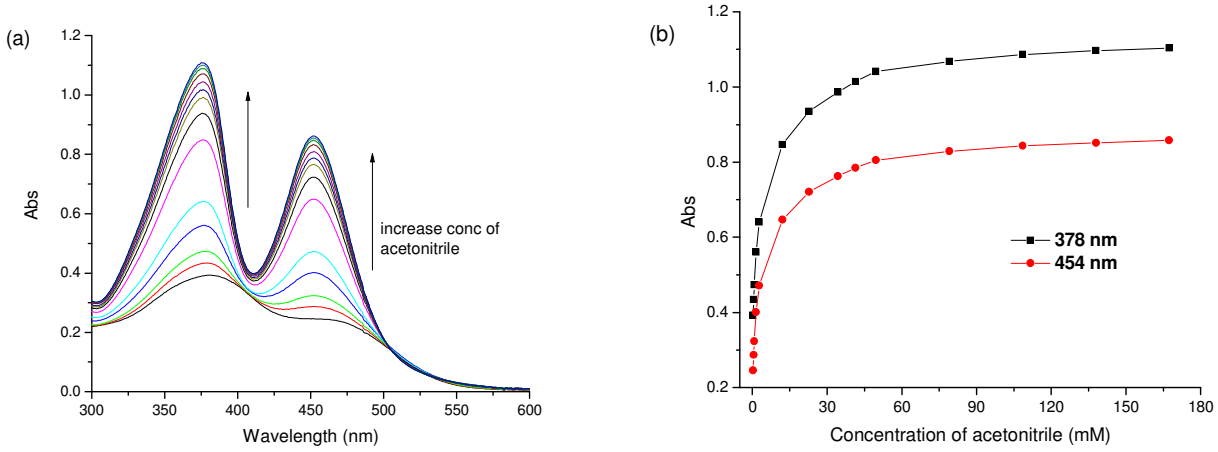

Figure S 14 (a) UV/Vis absorption titration plots for **1** in water and with addition of acetonitrile. (b) Changes in the absorbance at λ_{max} 378 nm and 454 nm.

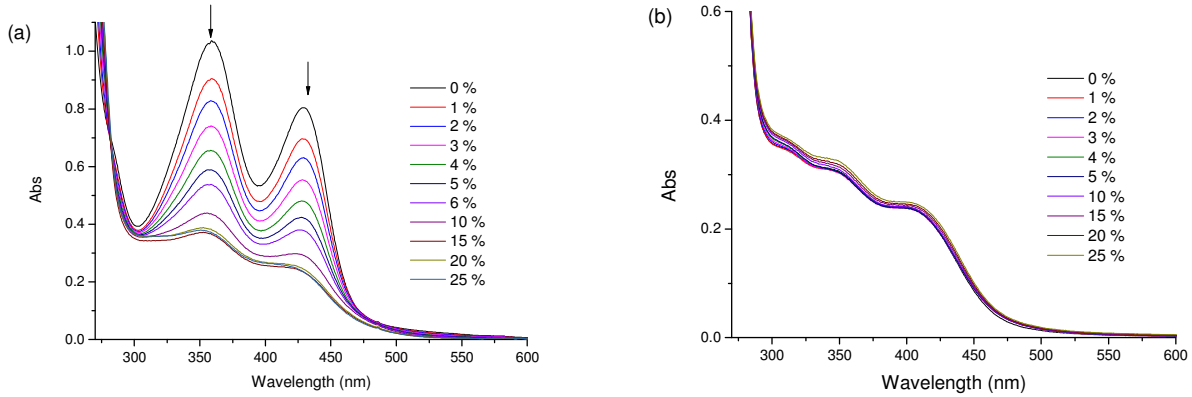

Figure S 15 UV/Vis titration plots **3** (a) in acetonitrile and with addition of water (in vol%) and (b) in water and with addition of acetonitrile (in vol%).

Table S2 UV/Vis absorption spectral data for **1**, **2** and **3** in acetonitrile and water.

	Acetonitrile		Water pH 6	
	Band II	Band I	Band II	Band I
1	378 nm (ε = 7400)	454 nm (ε = 5980)	378 nm (ε = 2890)	453 nm (ε = 2040)
2	380 nm (ε = 6750)	458 nm (ε = 5250)	387 nm (ε = 5570)	480 nm (ε = 4070)
3	359 nm (ε = 5050)	429 nm (ε = 4200)	347 nm (ε = 1300)	408 nm (ε = 1020)

ε in M^{-1} cm^{-1}

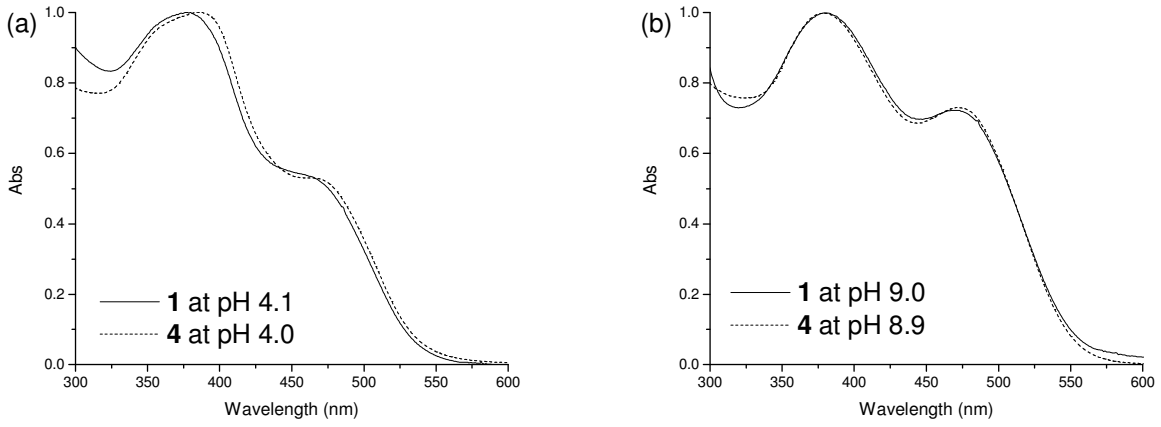

Figure S 16 UV/Vis spectra of **1** and **4** in water at ca. pH 4 and pH 9.

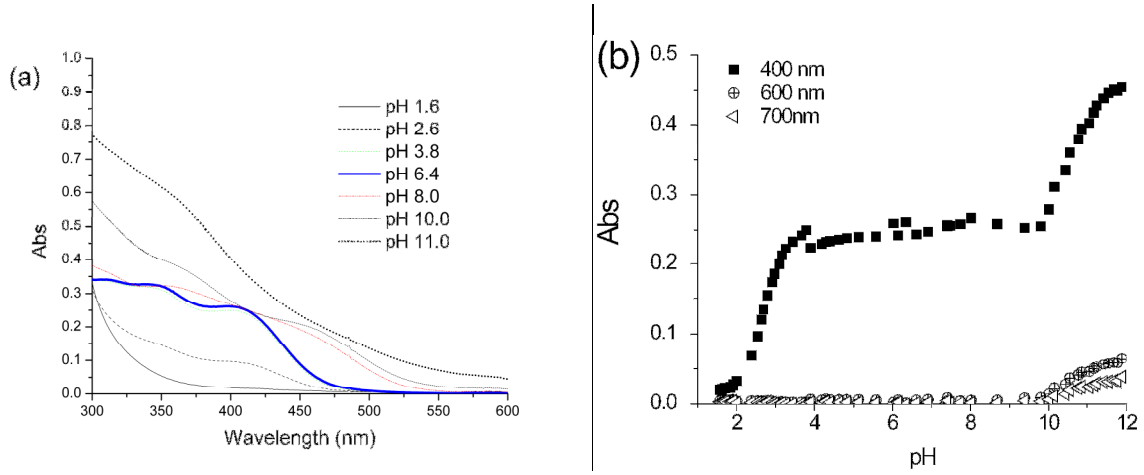

Figure S 17 pH dependence of the absorption spectra of (a/b) **3** in water. The broad increase in absorption observed at pH values above 8 is due to the formation of a precipitate causing scatter.

6. Resonance Raman Spectroscopy

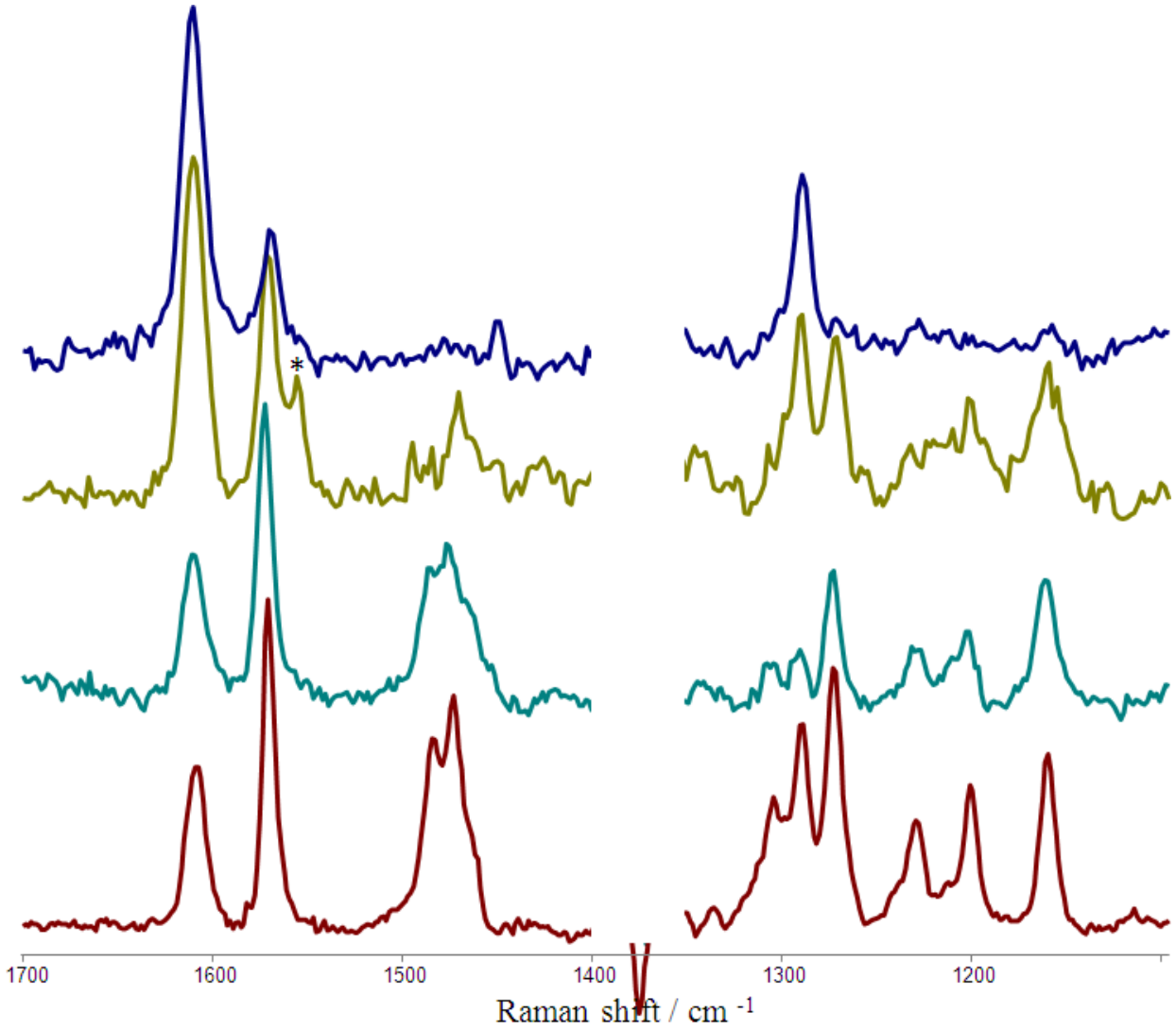

Figure S 18 Resonance Raman spectra of **1** (0.1 mM) in acetonitrile at λ_{exc} (from top to bottom) 355, 400.8, 449 and 473 nm. The region with distortion due to incomplete subtraction of solvent bands is masked. * indicates a spectral artifact.

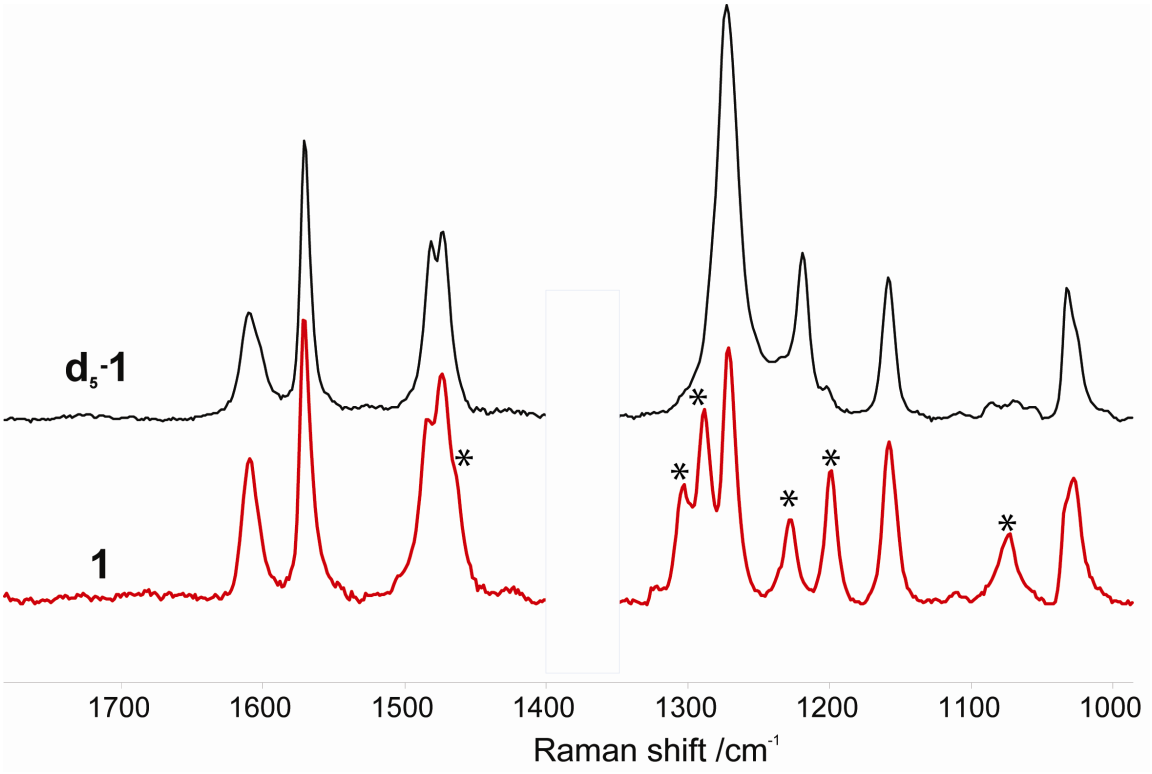

Figure S 19 Resonance Raman spectra of **1** and **d_5-1** in acetonitrile at 0.1 mM (at λ_{exc} = 473 nm). The region with distortion due to incomplete subtraction of solvent bands is masked. * denotes bands assigned to the alkyl amine modes.

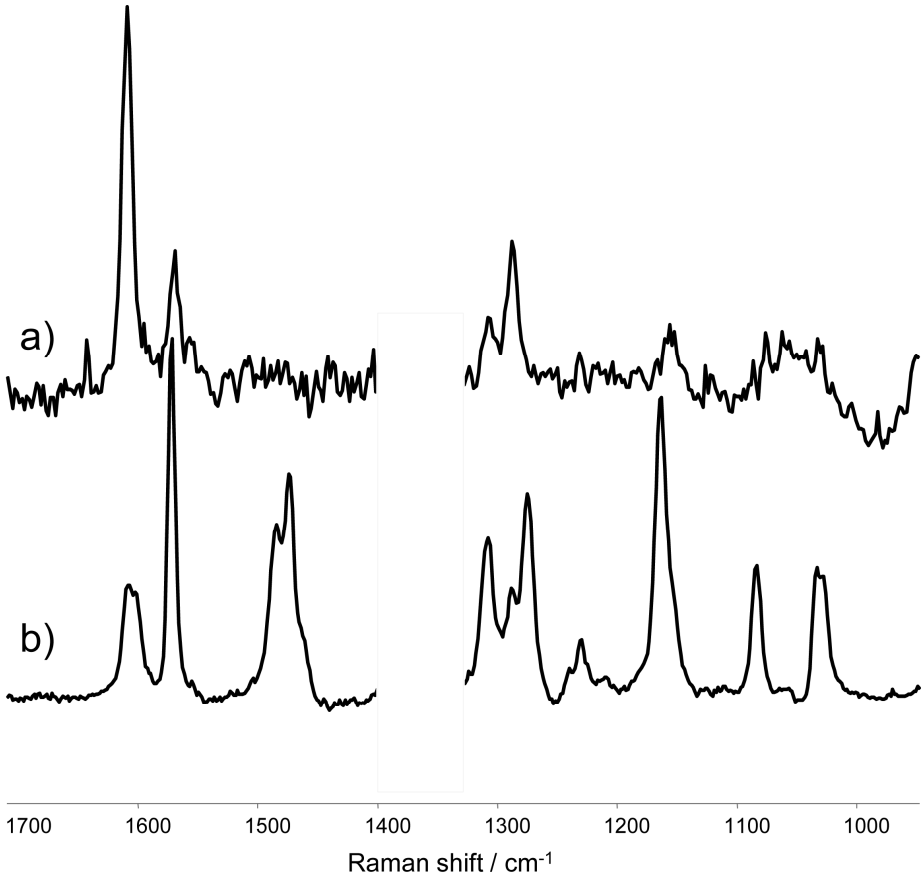

Figure S 20 Resonance Raman spectra of **2** (0.1 mM) in acetonitrile at λ_{exc} (a) 355 and (b) 473 nm. The region with distortion due to incomplete subtraction of solvent bands is masked.

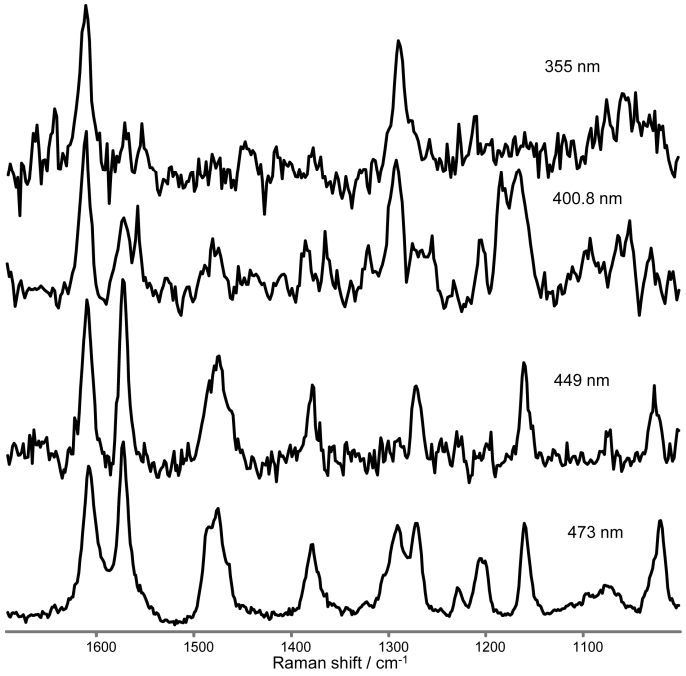

Figure S 21 Wavelength dependence of the resonance Raman spectra of **1** (0.5 mM) in water (pH 7.6).

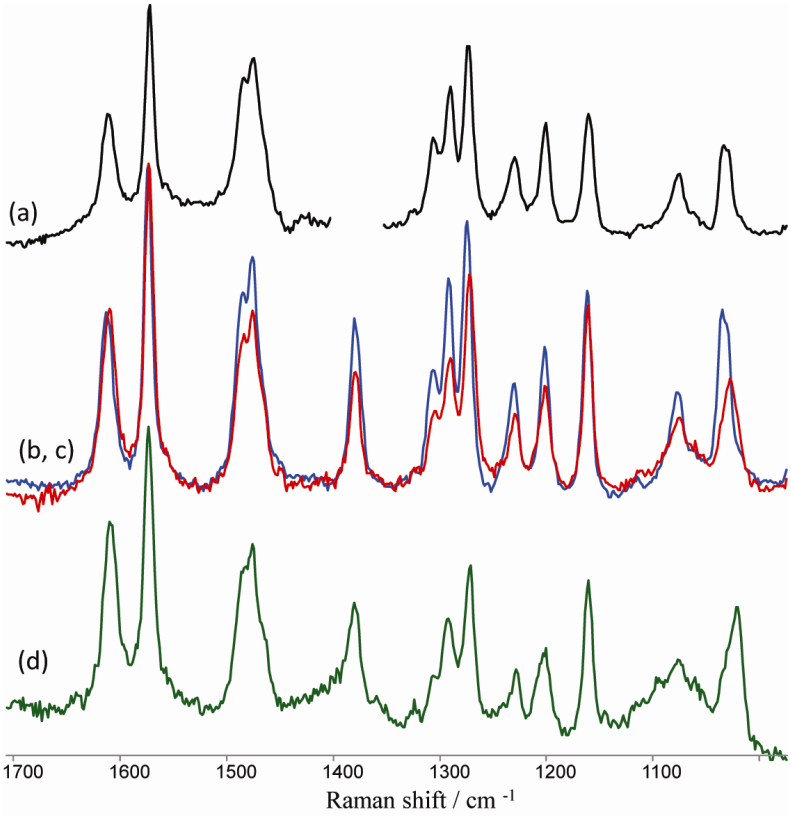

Figure S 22 Resonance Raman spectra at λ_{exc} 473 nm of the **1** (a) in acetonitrile (black), (b) in water (pH 7, red) at 0.5 mM, (c) after addition of 1 vol% of acetonitrile to the aqueous solution of **1** (blue) and (d) after addition of NaCl (0.1 M) (green). The region in (a) with distortion due to incomplete subtraction of solvent bands is masked.

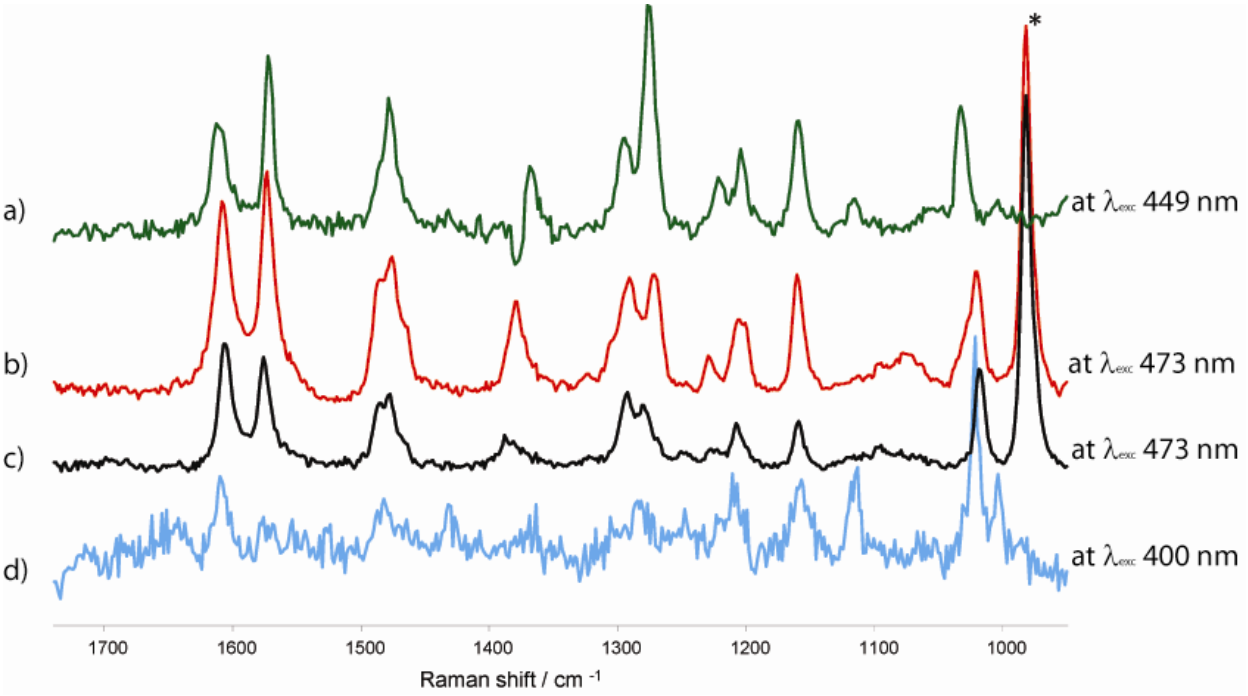

Figure S 23 Resonance Raman spectra at of (a) **3** (0.1 mM) in acetonitrile, (b) **1** (0.5 mM) in water pH 7.6, (c) **1** (0.5 mM) in water pH 9.1 and (d) **3** (0.5 mM) in water pH 6.5. * mode of SO_4^{2-}.

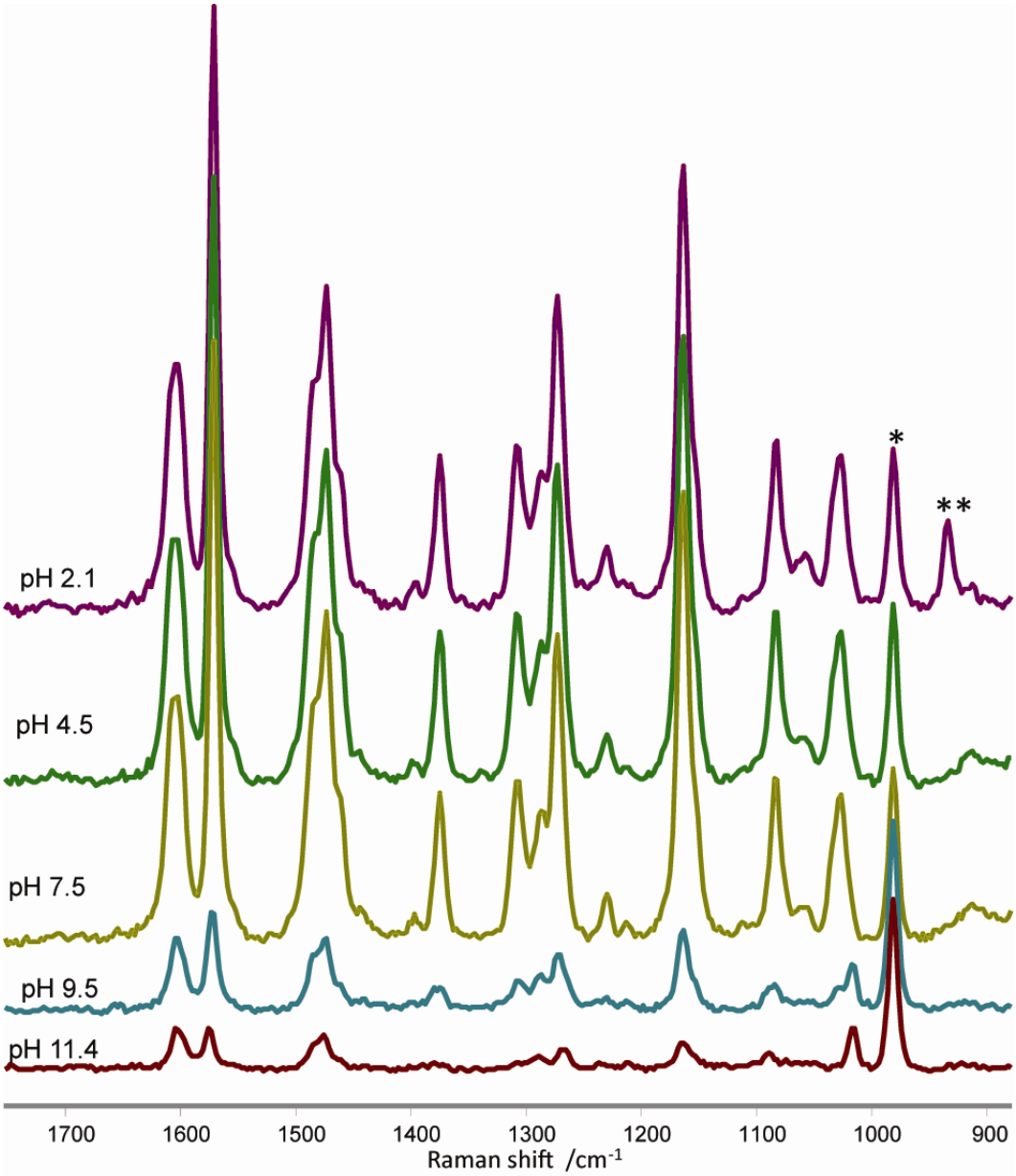

Figure S 24 Resonance Raman spectra of **2** (0.3 mM) in water pH at 2.1, 4.5, 7.5, 9.5 and 11.4 at λ_{exc} 473 nm excitation wavelength (spectra are normalized to the SO_4^{2-} band at 981 cm^{-1} (0.05 M Na_2SO_4 internal reference, * mode of SO_4^{2-}, ** mode of ClO_4^-). For the UV/vis absorption spectra of the solutions used in each case see Figure 7a.

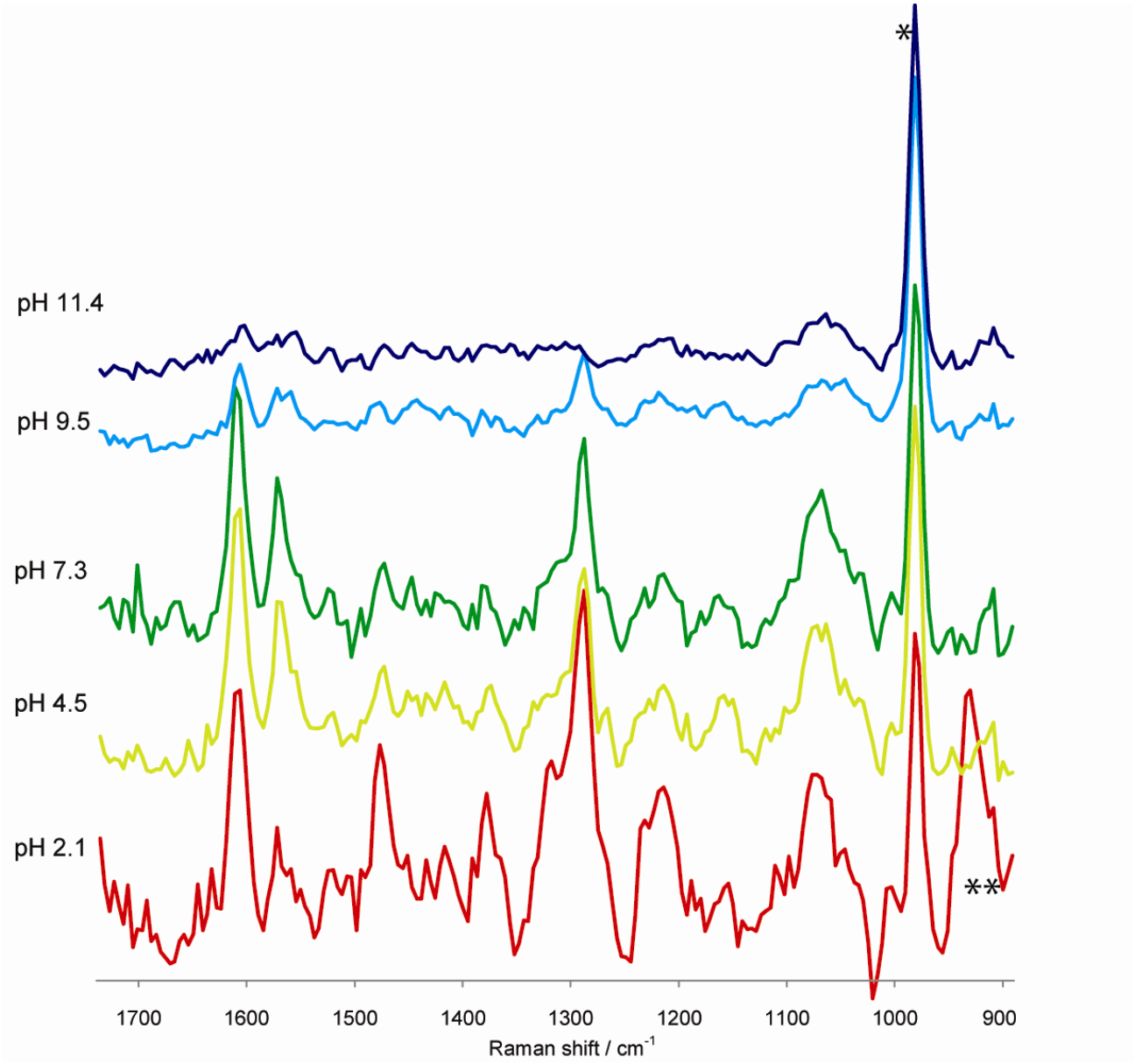

Figure S 25 Resonance Raman spectra of **2** (0.3 mM) in water pH at 2.1, 4.5, 7.3, 9.5 and 11.4 at λ_{exc} 355 nm excitation wavelength (spectra are normalized to the SO_4^{2-} band at 981 cm^{-1} (0.05 M Na_2SO_4 internal reference, * mode of SO_4^{2-}, ** mode of ClO_4^-). The UV/vis absorption spectra of the solutions used in each case are shown in Figure 7a.

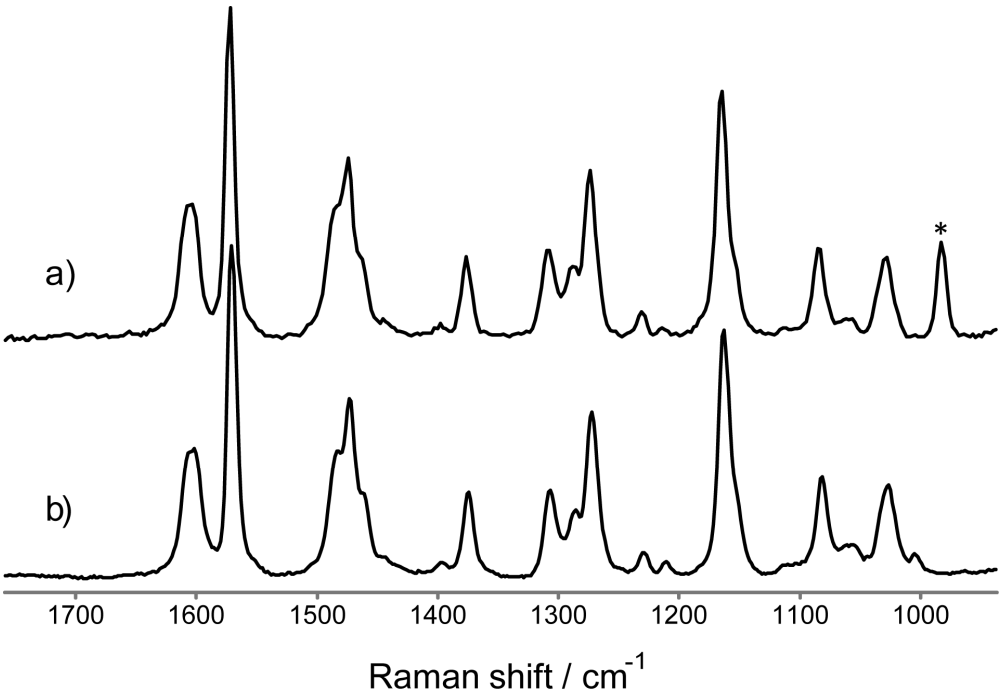

Figure S 26 Resonance Raman spectra at λ_{exc} 473 nm of (a) **2** in water (pH 7, black), 0.3 mM. and (b) MeN4Py and $FeSO_4$. * mode of SO_4^{2-}.

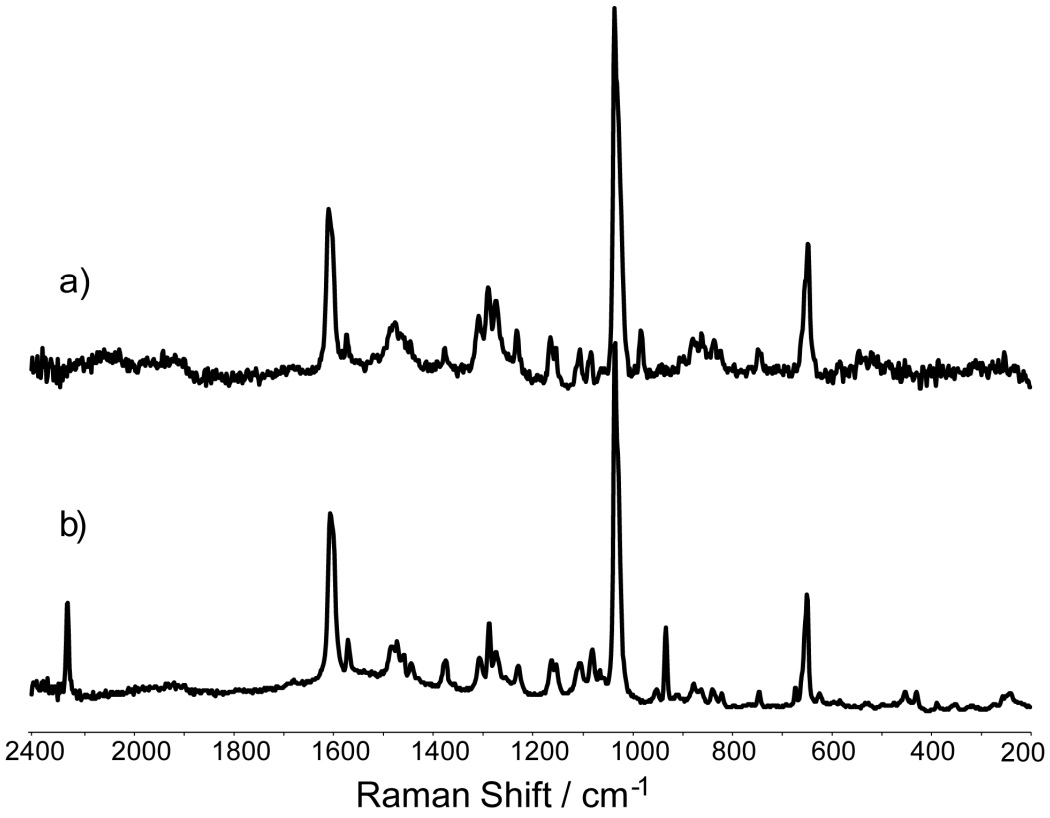

Figure S 27 Raman spectra at λ_{exc} 785 nm of (a) a 1 M solution of MeN4Py and $FeSO_4$ in water and (b) solid state Raman spectrum of **2**.

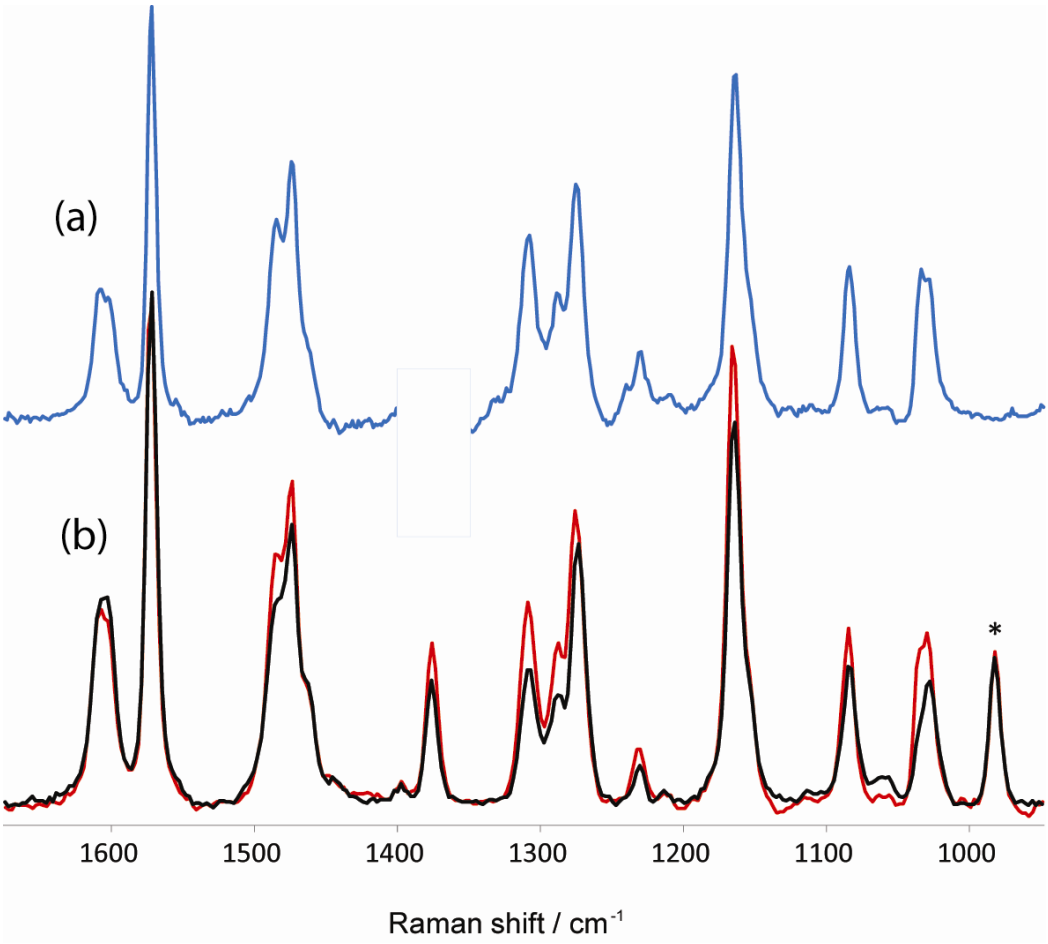

Figure S 28 Resonance Raman spectra at λ_{exc} 473 nm of the **2** (a) in acetonitrile (blue) and (b) in water (pH 7.5, black) at 0.3 mM and after addition of 1 vol% of CH_3CN to the aqueous solution of **2** (red).* mode of SO_4^{2-}. The region in (a) with distortion due to incomplete subtraction of solvent bands is masked.

7. Electrochemistry

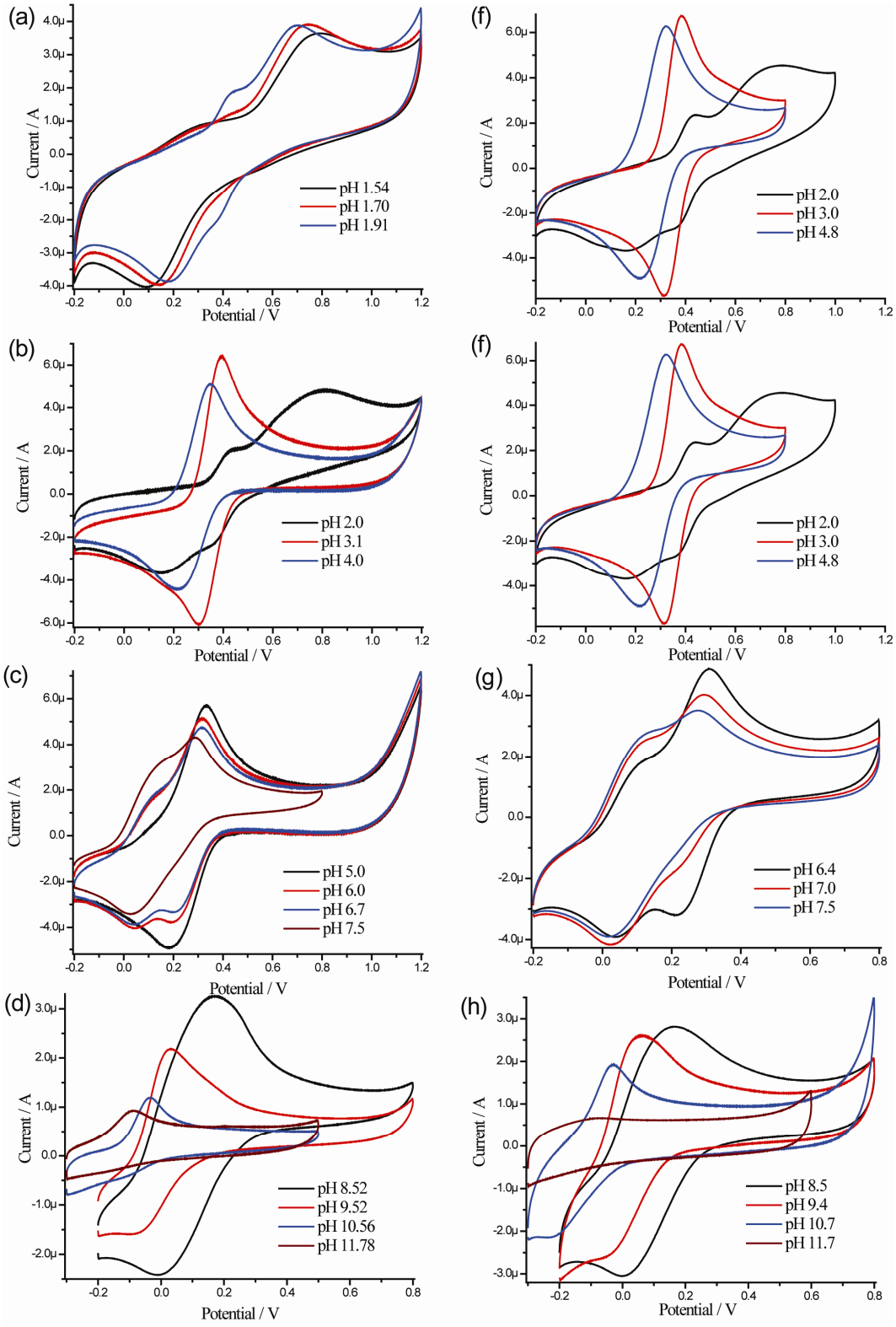

Figure S 29 Cyclic voltammograms of **1** (a-d) and of **4** (e-h) in water (10 mM KNO_3) between pH 1.5 and pH 12. All complexes are 0.5 mM. Scan rate: 0.1 V s^{-1}, vs SCE.

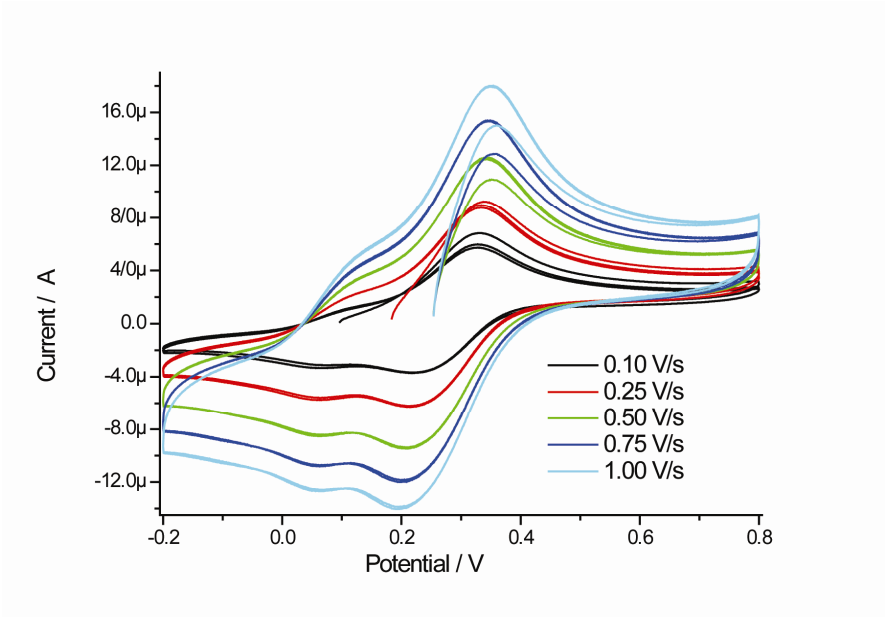

Figure S 30 Scan rate dependence of the cyclic voltammetry of **1** (0.5 mM) in water (10 mM KNO_3, vs SCE).

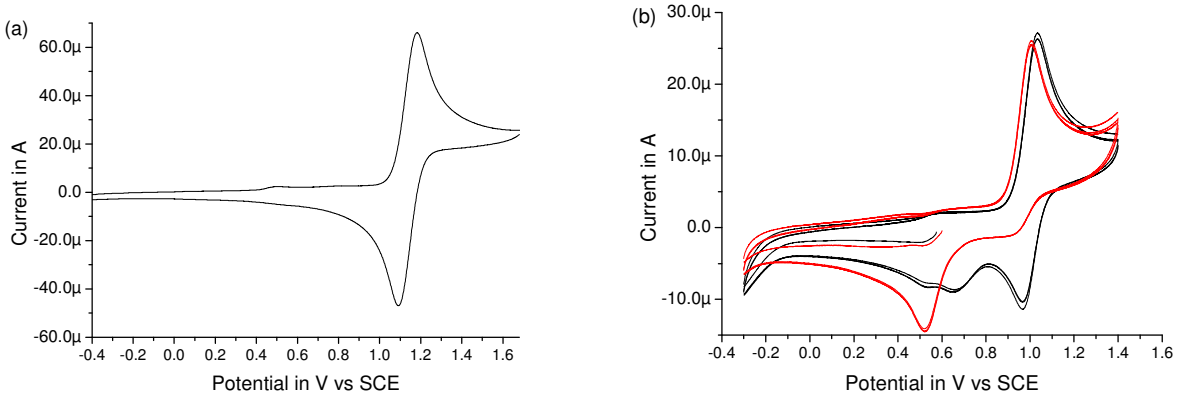

Figure S 31 Cyclic voltammetry of **2** (a) in acetonitrile (b) in acetonitrile with 1 vol% (black) and 10 vol% (red) water (0.1 M $TBAPF_6$, scan rate 0.1 V s^{-1}).

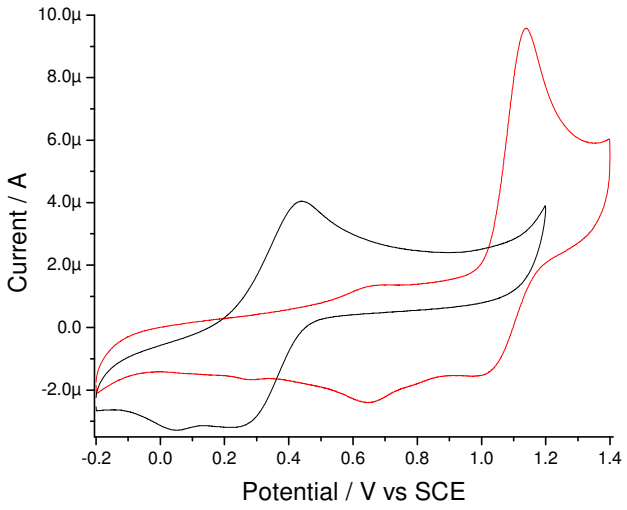

Figure S 32 Cyclic voltammograms of **3** (0.5 mM) in acetonitrile (red, 0.1 M $TBAPF_6$) and in water (black, 10 mM KNO_3) (scan rate 0.1 V s^{-1}).

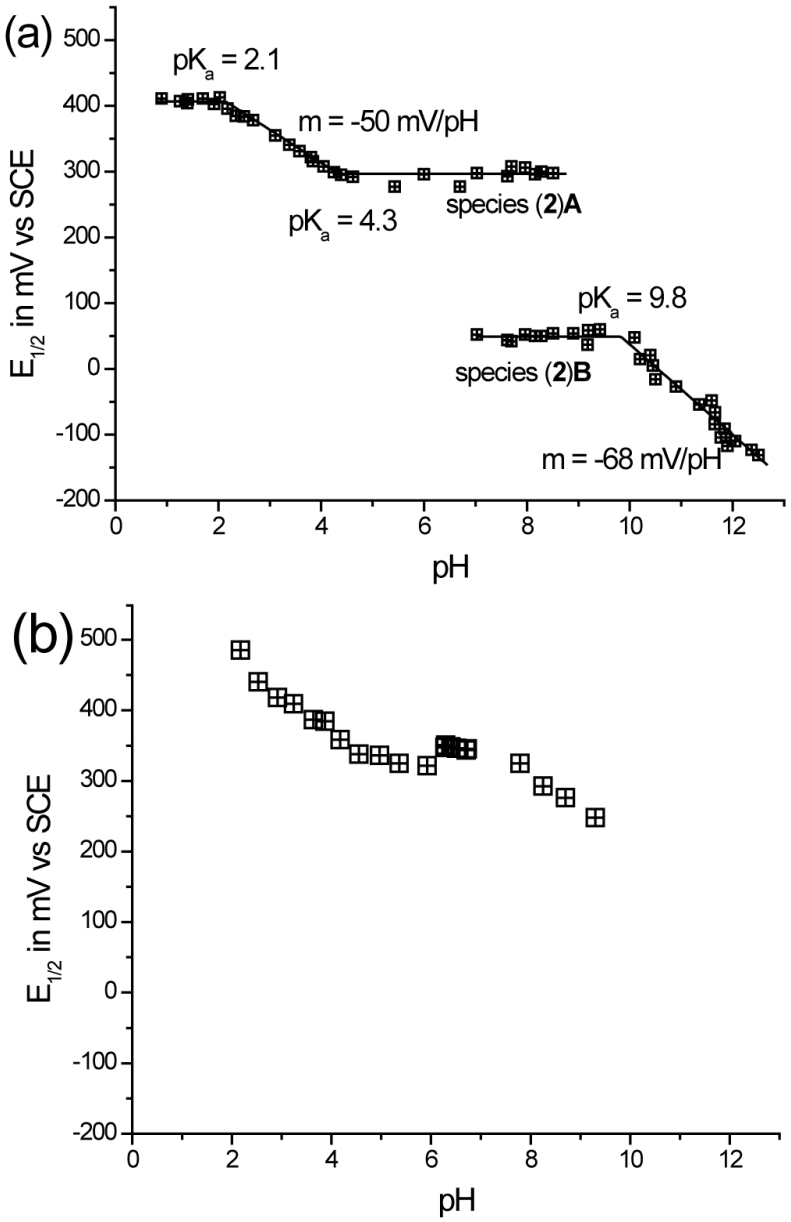

Figure S 33 Pourbaix plot for (a) **2** and (b) **3** in water (10 mM KNO_3).

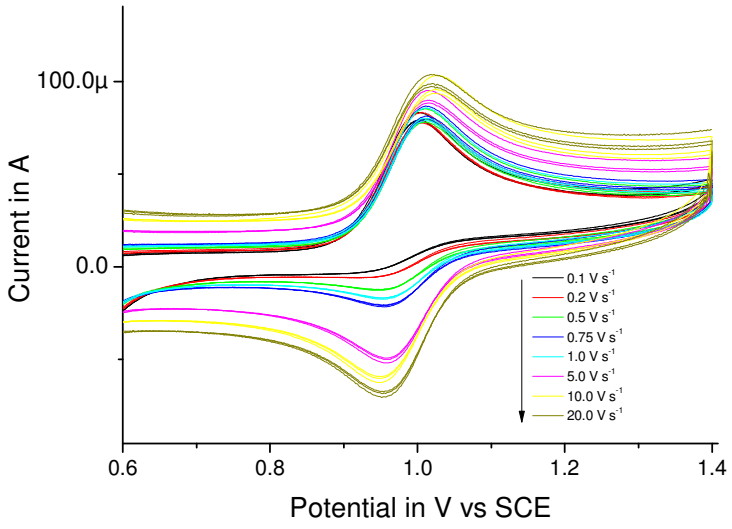

Figure S 34 Cyclic voltammetry of **2** (0.5 mM) in acetonitrile with 10 vol% water (0.1 M $TBAPF_6$, scan rate 0.1 to 20 V s^{-1}). Voltammograms are normalized to the (scan rate)^{½}. It should be noted that the scan rate dependence of **2** in acetonitrile with water added confirms that the aquation of the Fe^{III}-$NCCH_3$ complex follows electron transfer i.e. an EC mechanism.

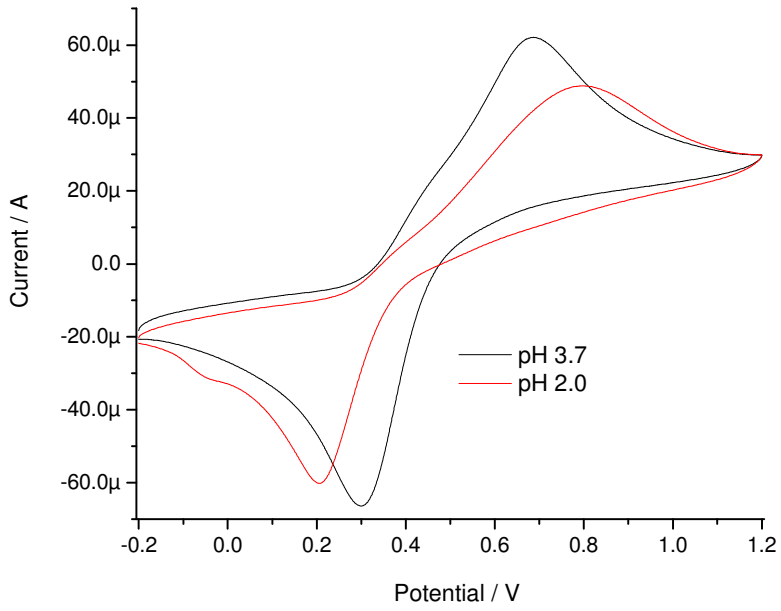

Figure S 35 Cyclic voltammetry of $FeSO_4$ (1 mM) in water at pH 3.7 and pH 2.0 (scan rate 0.1 V s^{-1}), vs SCE.

8. pH jumping experiments

The reversibility of the ligand dissociation and the interconversion between species **A** and species B were determined by pH jumping experiments.

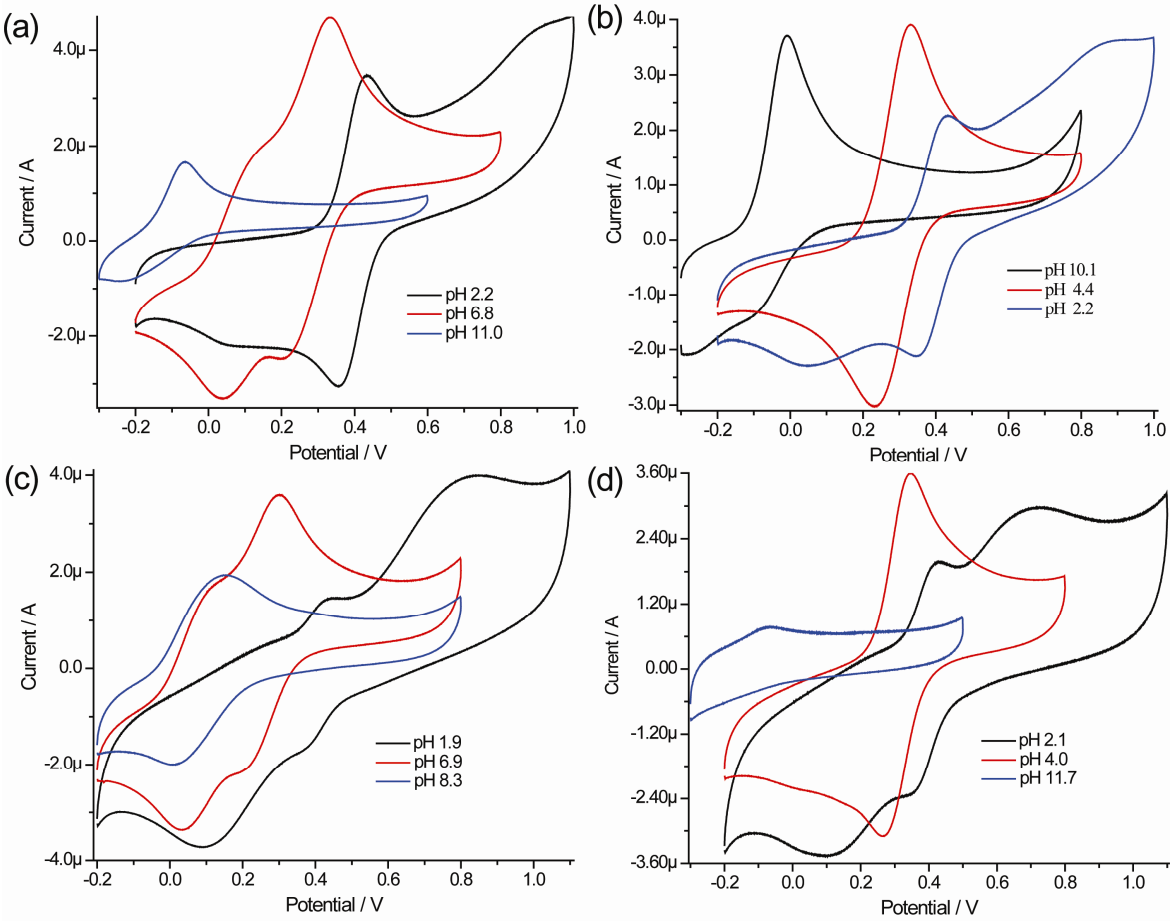

Figure S 36 pH jumping experiments (a) **1** in water pH from 6.8 to 2.2 to 11.0 (b) **1** in water pH from 10.2 to 4.4 to 2.2 (c) **4** in water pH from 6.9 to 1.9 to 8.3 (d) **4** in water pH from 11.7 to 2.1 to 4.0. The solutions were held at each pH value for several minutes before pH was adjusted again; potentials are vs SCE. Complexes are 0.5 mM. Scan rate 0.1 V s^{-1}.

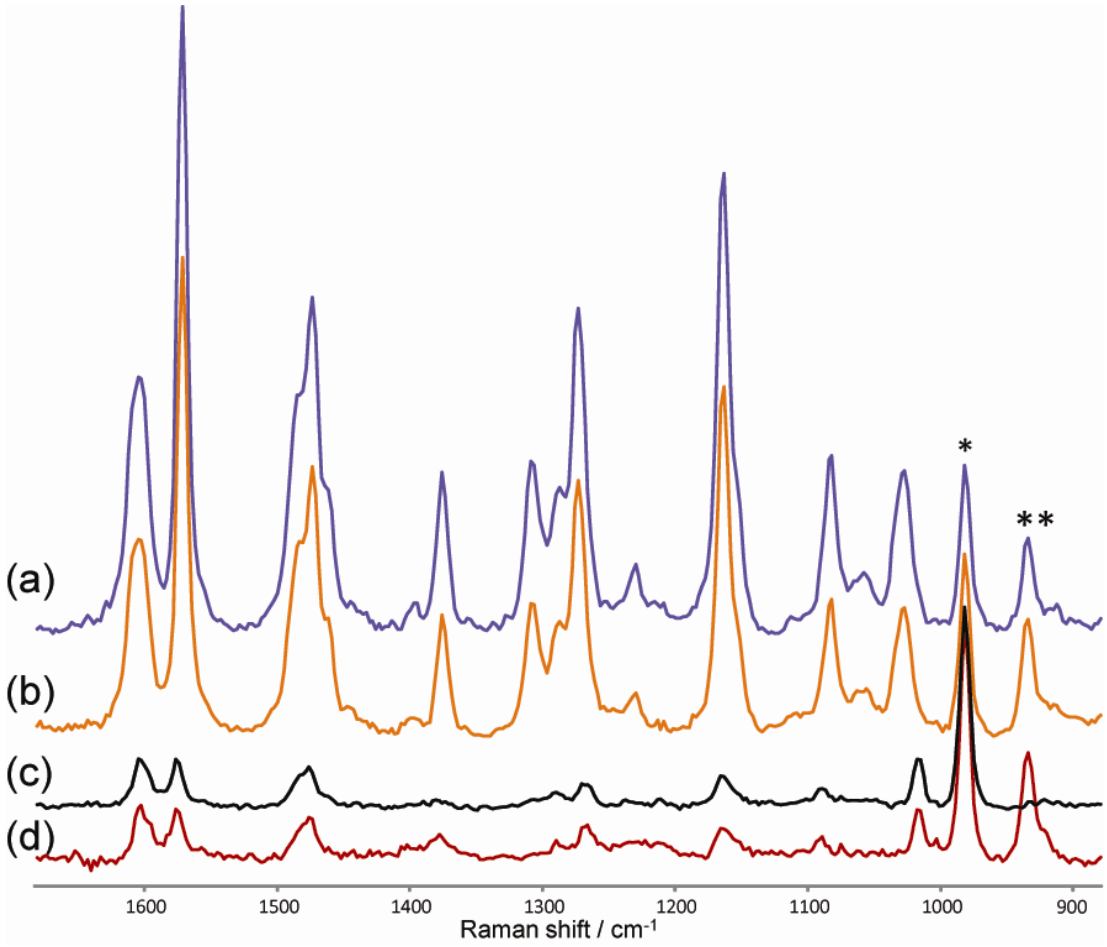

Figure S 37 pH jumping experiments followed by resonance Raman spectroscopy at 473 nm (a) **2** in water at pH 2.1 (b) **2** in water at pH 2.0 {after solution was first brought to pH 11.4}, (c) **2** in water at pH 11.4 and (d) **2** in water at pH 11.4 {after solution was first brought to pH 2.1}. (0.05 M Na_2SO_4 internal reference, * mode of SO_4^{2-}, ** mode of ClO_4^-.

9. Mass spectrometry

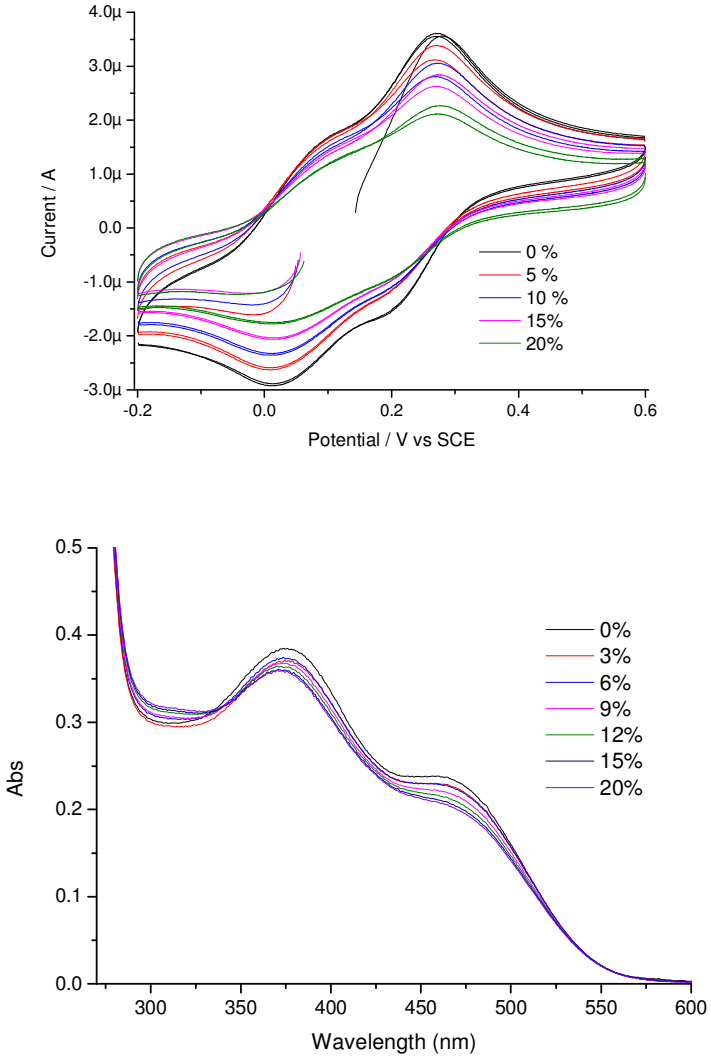

Figure S 38 (upper) Cyclic voltammetry and (lower) UV/Vis absorption spectrum of **1** (0.5 mM) in water, with increasing amounts of ^{t}BuOH (vol%) (UV/Vis absorption spectra are corrected for dilution). Note that the change in peak current is concomitant with the change in the background non-faradaic current as the concentration of ^{t}BuOH is increased; there are no additional redox waves observed.

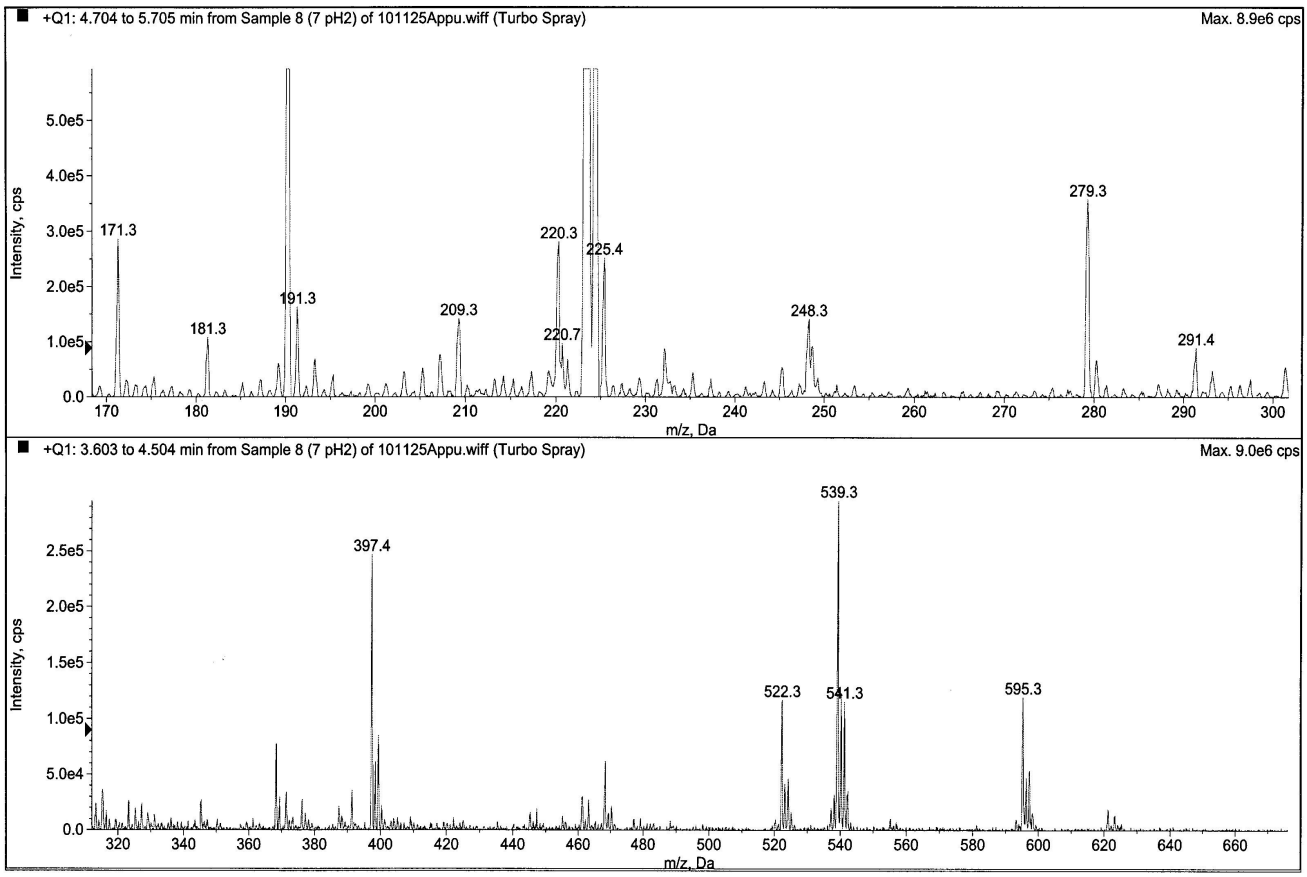

Figure S 39 ESI-MS spectrum of **1** at pH 2 in ^{t}BuOH/H_2O (1:4 v/v), dilute $H_2SO_{4(aq)}$ and $NaOH_{(aq)}$ were used to adjust pH.

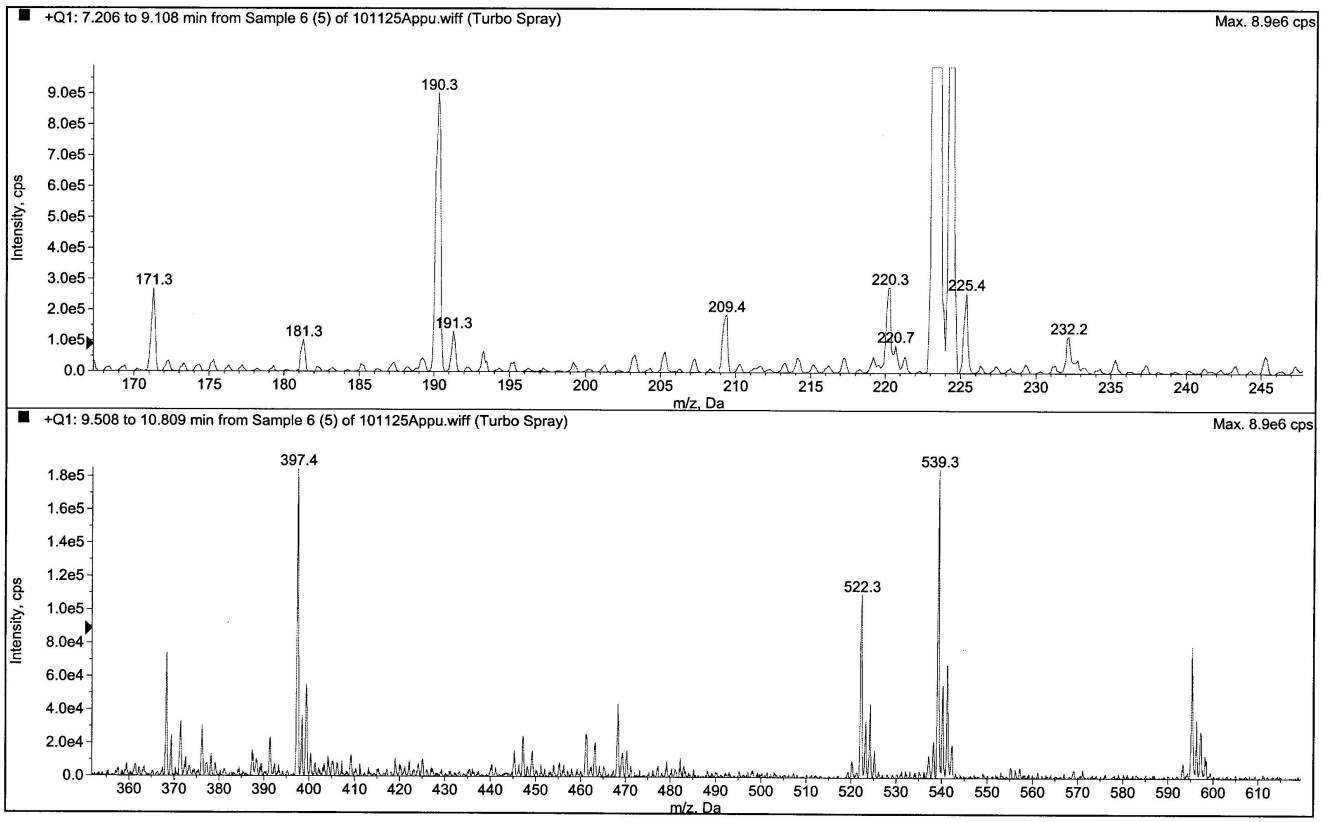

Figure S 40 ESI-MS spectrum of **1** at pH 6 in $^{t}BuOH/H_2O$ (1:4 v/v), dilute $H_2SO_{4(aq)}$ and $NaOH_{(aq)}$ were used to adjust pH.

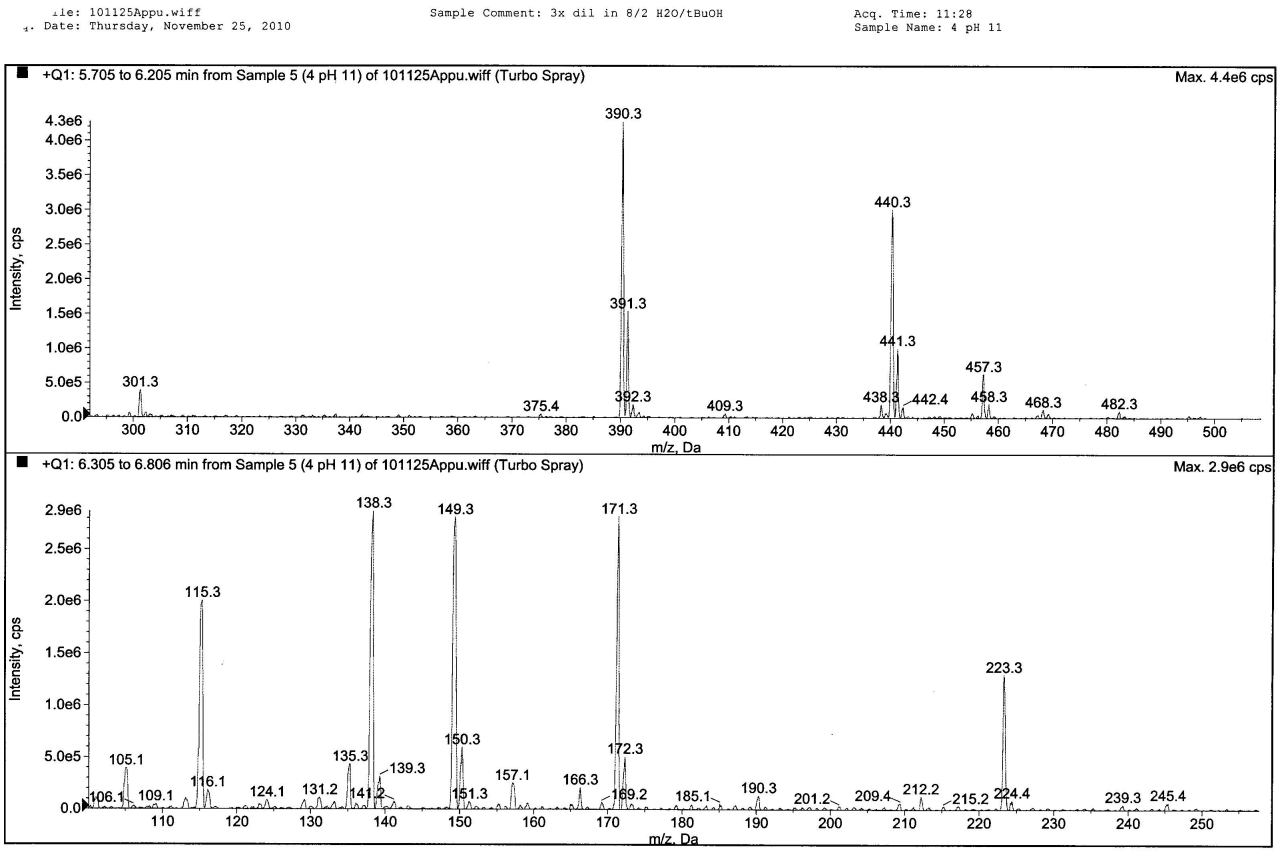

Figure S 41 ESI-MS spectrum of **1** at pH 11 in ^{t}BuOH/H_2O (1:4 v/v), dilute $H_2SO_{4(aq)}$ and $NaOH_{(aq)}$ were used to adjust pH.

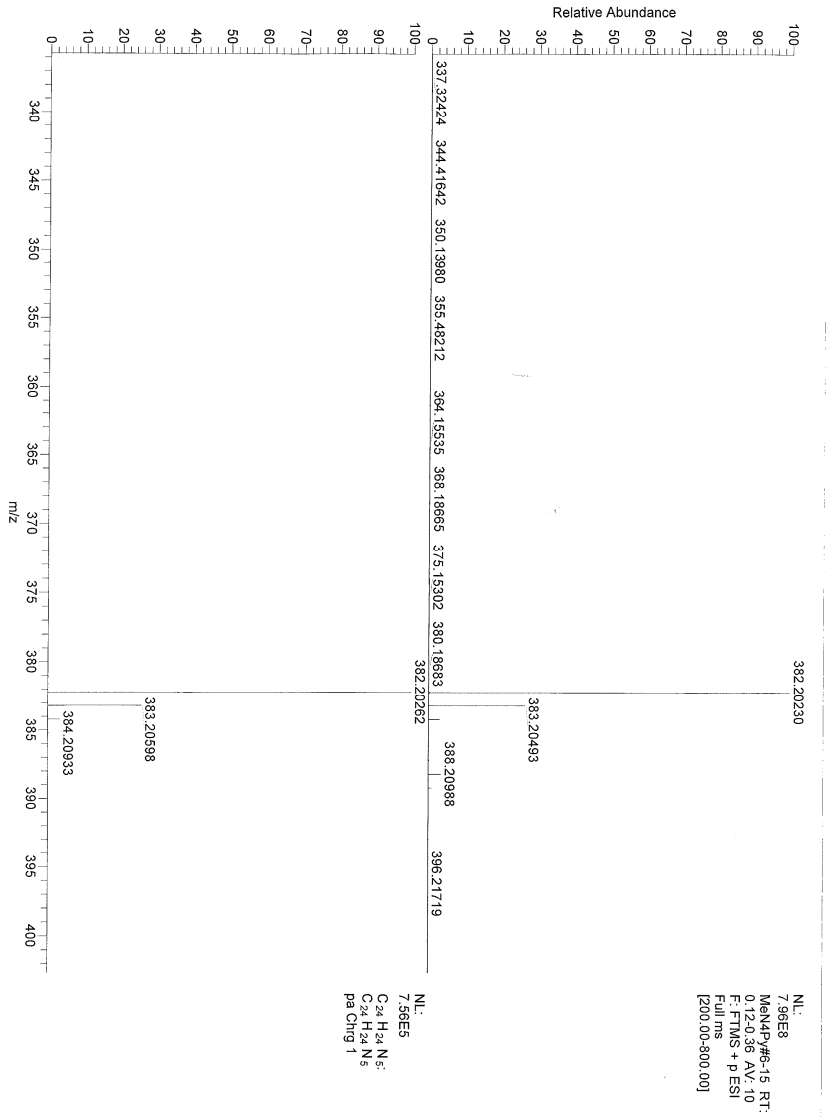

Figure S 42 ESI-MS spectrum of MeN4py

---

(1) Gerard Roelfes, G.; Lubben, M.; Chen, K.; Ho, R Y. N.; Meetsma A.; Genseberger, S.; Hermant, R. M.; Hage, R.; Mandal, S. K.; Young, V. G. Jr.; Zang, Y.; Kooijman, H.; Spek, A. L.; Que, L. Jr.; Feringa, B. L. *Inorg. Chem*. **1999**, *38*, 1929-1936.

(2) McClanahan, S.; Kincaid, J. *J. Raman Spectro.* **1984**, *15*, 173-178.

(3) The isotope shifts are observed in the FTIR spectra also, see SOI Figures S2 and S3.